

FLOW ENABLED SELF ASSEMBLY OF POLYMERS

A Thesis
Presented to
The Academic Faculty

by

Chuchu Zhang

In Partial Fulfillment
of the Requirements for the Degree
Master of Science in the
School of Materials Science and Engineering

Georgia Institute of Technology
May 2016

COPYRIGHT © CHUCHU ZHANG 2015

FLOW ENABLED SELF ASSEMBLY OF POLYMERS

Approved by:

Dr. Zhiqun Lin, Advisor
School of Materials Science and Engineering
Georgia Institute of Technology

Dr. Vladimir Tsukruk
School of Materials Science and Engineering
Georgia Institute of Technology

Dr. Valeria Milam
School of Materials Science and Engineering
Georgia Institute of Technology

Date Approved: [Dec 16, 2015]

To my parents

ACKNOWLEDGEMENTS

I would like to thank everyone that has helped and supported me throughout the past two years in Tech. First of all, I would thank my advisor Prof. Zhiqun Lin, for his guidance and support. It was an interesting experience to work with him and his encouragement is essential to the completion of this project. I would also like thank my committee members, Prof. Vladimir Tsukruk and Prof. Valeria Milam, for their considerable participation and valuable understanding.

Special thanks are extended to the current and former Nano FM group members. Dr. Bo Li has been a great mentor, and it was him that guided me to the world of coffee ring and to set up serious research. I really appreciate his help and innovative insight to both experimental and theoretical part of the project. Furthermore, I'm grateful for the valuable mentorship provided by Dr. Xinchang Pang and Dr. Ming He. Working with them has been a fantastic learning experience. I would like to thank PhD candidate Beibei Jiang, PhD candidate Yanjie He, PhD candidate James Iocozzia and Dr. Chaowei Feng for their encouragement and help in many occasions especially characterization technique trainings. I would also like to thank Dr. Jeahan Jung, Young Jun, Zewei Wang, Yuwei Han and other group members for their support.

I was privileged to collaborate with excellent researchers in my master period. Among which I would especially thank Dr. Yijie Tao, who brought his amazing electrochromic polymer synthesis and characterization technique to the group during his visit and inspired me a lot in the work of fabricating electrochromic grating. Another special thank goes to PhD candidate Liyi Li. He has been really considerable and helpful

in the collaboration of microchanel project and helped in SEM and AFM characterization. I'm also blessed to meet Dr. Wentian Gu, Dr. Xiaxi Li, Congshan Wan, Liang He, Ziyu Zhou and many other friends in Tech who provide constant encouragement and support. The faculty and staff members at Graduate office of School of Materials Science and Engineering should also be especially thanked for their help in assisting the whole process of earning the degree.

Finally, I would like to thank my parents. They always trust and support me no matter what. They are the source of my courage and happiness. I would also like to thank my boyfriend for always having my back.

TABLE OF CONTENTS

	Page
ACKNOWLEDGEMENTS	iv
LIST OF FIGURES	viii
LIST OF SYMBOLS AND ABBREVIATIONS	xi
SUMMARY	xii
 <u>CHAPTER</u>	
1 INTRODUCTION	1
1.1 Evaporation Induced Self Assembly	2
1.2 Mechanism and Theoretical Model of “Coffee Ring” Effect	6
1.3 Crafting Highly Ordered Structure via Flow-Enabled Self-Assembly	19
1.4 System Setup and Parameters of FESA	22
1.5 Research Objective	25
2 MECHANISM STUDY OF POLYSTYRENE PATTERNS CRAFTED BY FLOW-ENABLED SELF-ASSEMBLY	26
2.1 Introduction	26
2.2 Results and Discussion	31
2.3 Experimental	44
2.4 Conclusion	46
3 APPLICATIONS OF FLOW-ENABLED SELF-ASSEMBLY	48
3.1 Introduction	48
3.2 Facile Patterning of Donor-Acceptor Electrochromic Polymer via Flow-Enabled Self-Assembly	49
3.3 Silicon Microchannels and Microgratings Templated by Flow-Enabled	

Self-Assembly	55
4 CONCLUSIONS	64
4.1 Thesis Review	64
4.2 Future Work	65
REFERENCES	66

LIST OF FIGURES

	Page
Figure 1.1: “Coffee-ring” phenomenon	2
Figure 1.2: Schematic of Deegan’s coffee-ring effect mechanism model	3
Figure 1.3: Photographs of deposit from evaporating drops of 0.1 μ m microsphere suspension at various concentrations	4
Figure 1.4: Typical curved-on-flat geometric restrictions, “sphere-on-flat” in particular	5
Figure 1.5: Schematic for spherical cap approximation	8
Figure 1.6: Numerical evaporation flux j versus radial coordinate r results of water drop calculated by a) Lens model; b) NEOS model. The dash lines are the corresponding drop profile	10
Figure 1.7: Local evaporation rate versus non-dimensionalized r [-]	11
Figure 1.8: Representative velocity vectors and streamlines for pinned droplet	13
Figure 1.9: Radial a) and vertical b) component of the velocity of evaporative flux at different relative radial position	14
Figure 1.10: “Tears of wine”	15
Figure 1.11: Flow field images a) taken from experiment and b) from theoretical prediction of evaporating octane droplet.	16
Figure 1.12: Patterns formed after evaporation of suspensions with different shape and close-up images of the particles near the contact line	18
Figure 1.13: Schematic for a) Slot coating and b) flow coating	20
Figure 1.14: Crafting hierarchical structures of PS-b-P4VP micelles and threads using FESA technique	21
Figure 1.15: Macroscopic high aligned ultra-long DNA nanowires via FESA technique and its convections into metal nanowires	22
Figure 1.16: Schematic for key parts of flow-enabled self-assembly (FESA) setup	23
Figure 1.17: A complete setup for flow-enabled self-assembly	25

Figure 2.1: Schematic of CESA setup a), optical micrograph and AFM mapping of CESA pattern by: b-c) PS-60K; d-e) PS-112K; f-g) PS-420K in toluene. Concentration c is 0.25mg/mL. Scale bar = 70 μ m.	27
Figure 2.2: Patterns transformation depending on different moving speed of the substrate	29
Figure 2.3: Qualitative analysis of effect of surface pressure and transfer velocity	30
Figure 2.4: Schematic and optical micrographs of evaporation-induced patterns at different evaporative stage of 15 μ L PS toluene solution	33
Figure 2.5: A collection of patterns created from FESA of 112 K-PS toluene solution at the concentration of 4.4g/L with different moving velocity v	34
Figure 2.6: Phase diagram of 112K PS toluene solution on Si wafer depending on initial concentration and lower plate moving velocity according to optical microscopic observations	35
Figure 2.7: Phase diagram of 1g/L PS toluene solution on Si wafer depending on moving speed and molecular weight of PS according to optical microscopy observation	36
Figure 2.8: a) sketch and b) experimental result of the formation of fingering instability. Viscous flow is released on an inclined plane, and fingers are developed driven by gravity	37
Figure 2.9: a) Molecular weight dependence and concentration dependence of intrinsic viscosity of PS toluene solution	39
Figure 2.10: Relationship between the spacing of spokes generated from fingering instability and: a) the velocity of the lower plate (MW=112K, c=2g/L); b)-red, Molecular weight ($v=0.003$ mm/s, c = 1g/L) and b)-black concentration (MW=112k, $v=0.003$ mm/s).	40
Figure 2.11: Relationship between the spacing of two adjacent strips and the velocity of the lower plate for 1M 876K PS toluene solution	42
Figure 2.12: Relationship between the spacing of two adjacent strips and the velocity of the lower plate for the patterns formed from: a) 4M 112K PS toluene solution and b) 8M 112K PS toluene solution	42
Figure 2.13: Relationship between the pitch width and strip width for patterns formed(a, b) and the data fitting from Eq2.4(c, d) from: a) and c)1M 876K PS toluene solution; b)and d) PMMA toluene solution	44
Figure 3.1: Schematic of chemical structures of: a) Poly (Cz-HT-Tz); b) Poly (IDT-HT-Tz) and c) Poly (IDT-Tz)	50

- Figure 3.2: a) spin-coated Poly (Cz-HT-Tz) on ITO glasses under neutral, partially oxidized and completely oxidized condition after -0.4V, 0.8V, 1.1V voltage was applied respectively. b) Optical image and micrograph of patterned Poly (Cz-HT-Tz); c) UV-vis NIR spectroelectrochemistry of patterned Poly (Cz-HT-Tz). d) AFM image of patterned Poly (Cz-HT-Tz) strip. e) Profilometer result across an array of Poly (Cz-HT-Tz) strips. f) Interference patterns obtained using a green diode laser illuminating on a neutral patterned Poly (Cz-HT-Tz) film on ITO glass 52
- Figure 3.3: a) Optical images and micrographs of patterned Poly (IDT-HT-Tz) under neutral (-0.4V) and completely oxidized state (0.9V) on ITO glasses. b) UV-vis NIR Spectroelectrochemistry of patterned Poly (IDT-HT-Tz). c) AFM image of adjacently patterned Poly (IDT-HT-Tz) strips. d) Interference patterns obtained using a green diode laser illuminating on a neutral patterned Poly (IDT-HT-Tz) film on ITO glass. 53
- Figure 3.4: a) Optical image and micrograph of patterned Poly (IDT-Tz) under neutral (-0.4V) and completely oxidized state (0.9V) on ITO glasses. b) UV-vis NIR spectroelectrochemistry of patterned Poly (IDT-Tz). c) AFM image of a Poly (IDT-Tz) strip. d) Interference patterns obtained using a green diode laser illuminating on a neutral patterned Poly (IDT-Tz) film on ITO glass 54
- Figure 3.5: Optical images of patterned ECPs films on flexible substrate in neutral state (upper image) and oxidized state (lower image) 55
- Figure 3.6: 6 Schematic of photolithography-plasma etching route (a-d) and FESA-MaCE route for high aspect ratio microstructures fabrication on Si wafer (e-g) 58
- Figure 3.7: Schematic processing flows for dry etching (left) and MaCE (right) 59
- Figure 3.8: Optical micrograph of Si Surface after FESA patterning. 59
- Figure 3.9: AFM images of polymer strip after immersion in MaCE for a) 0 min; b) 10 min; c) 20 min; d) 60 min and e) their corresponding AFM cross sections profiles 60
- Figure 3.10: a-f) AFM images of patterned BCP strips after descum process of : a) 20 s; b) 60 s; c) 120 s; d) 180 s; e) 210 s and f) 240 s. The corresponding cross section profiles is shown in g), and the relationship between descum time and width (w_p) and height (h_p) of the strip is shown in h) 61
- Figure 3.11: Cross sectional SEM images of Si sample after FESA and MaCE for 10 with different descum time 63

LIST OF SYMBOLS AND ABBREVIATIONS

k_B	Boltzmann constant
T_s	Surface temperature
M_l	Molecular mass of liquid
ρ_s	Vapor density at the surface
ρ_v	Homogeneous vapor density
ρ_l	Vapor density of the liquid
j	Evaporation flux
D_m	Diffusion coefficient
θ	Contact angle
θ_c	Critical contact angle
γ	Surface tension
η	Viscosity of solution
λ_{c-c}	Center to center distance between strips
MW	Molecular weight
PS	Poly-Styrene
c	Concentration of injected solution
v	Moving speed of contact line (or lower plate)

SUMMARY

Self-assembly of nanoscale materials to form intriguing structures has garnered considerable attention due to their potential applications in optical, electronic, magnetic and information storage devices. Among all the efforts to pattern functional polymers and nanomaterials, flow-enabled self-assembly (FESA) stands out as a lithography-free evaporation induced self-assembly technique to construct large-scale 0D, 1D and 2D periodic structures in a simple, robust and cost effective manner. In the first part of my thesis, flow-enabled self-assembly of polystyrene is chosen as model system, and systematic experiments have been conducted to reveal intrinsic and external variables that lead to 3 possible FESA patterns. In the second part of my thesis, applications of FESA in patterning electrochromic polymers and fabricating PS-PMMA strips as etching mask of Si microchannels are demonstrated. The performance of the devices and the spacing of strips are characterized and compared to the existing patterning techniques.

CHAPTER 1

INTRODUCTION

Self-assembly refers to a spontaneous process for disordered materials to be organized into surface patterns (2D) or special structures (3D) without the application of external fields. The size of the resulting patterns or structures can vary from molecular level to planetary scale^[1]. In particular, self-assembly of functional nanoscale materials has attracted considerable interest ^[2-5] as it integrates unique material properties with desired hierarchical order structures in a low-cost yet high-yield way^[6], and on the other hand generate even more structural properties^[7-9]. To date, many efforts have been dedicated to use template-assisted strategies to assemble nano materials into intriguing hierarchical structures^[10, 11]. Although high resolution of patterns can be achieved by some of those lithographic methods, drawbacks such as high cost, procedure complexity and low yield in either template fabricating or the assembly steps are always not negligible. Therefore, alternative strategy which is capable of large-scale fabrication with simple operation process at lower cost is highly desirable. To this end, many effective techniques such as Langmuir-Blodgett (LB) Technique^[12-14], liquid-liquid interface self-assembly^[15-17], external field-assisted self-assembly^[18-20], evaporation induced self-assembly have been developed^[21, 22]. Among those alternatives, Evaporation induced self-assembly stands out for its ease of fabricating complex yet large scale structures at extremely low cost. In the following sections, mechanism and examples of evaporation induced self-assembly will be introduced in details. It also serve as good examples to elucidate that understanding the essence of self-assembly as well as material properties is essential to better and easier controlled self-assembly.

1.1 Evaporation-Induced Self-Assembly

When the nonvolatile solutes deposit on a solid surface during its solution evaporation process, self-assembled 1D or 2D structures can be maintained. This self-assembly system is called evaporation-induced self-assembly^[23]. The initial idea of evaporation-induced self-assembly comes from an interesting phenomenon – “coffee-ring” effect, which describes that drying coffee droplet will leave behind a ring-like structure rather than a condensed film on table, tissue or mug bottom(Fig 1.1)



Figure1.1 “Coffee-ring” phenomenon

This everyday seen phenomenon didn't really attracted physicists' interest until 1997, when Deegan proposed a decent model to explain that the ring-like structure is formed due to radial flow inside the droplet during evaporation^[24]. In a sessile droplet model, since the contact line – the line where substrate, solution and vapor meet – is pinned on the substrate (Fig1.2 a, b), the surface tension will increases and thus induce internal flow, which carry the suspended solute to the contact line and get deposited (Fig 1.2c). The coffee-ring effect is not exclusive to coffee solution. In fact, the ring-like structure has been widely detected and reported ^[25-27]. Coffee ring effect can be very annoying in some situation such as inject printing, which enhance the edges of colored area and lead to color distortion. On the other hand, however, the idea of understanding internal flux inside a

drying droplet and utilize it to rearrange the nonvolatile solute and get deposited inspired a novel lithography-free self-assembly method, i.e. evaporation induced self-assembly.

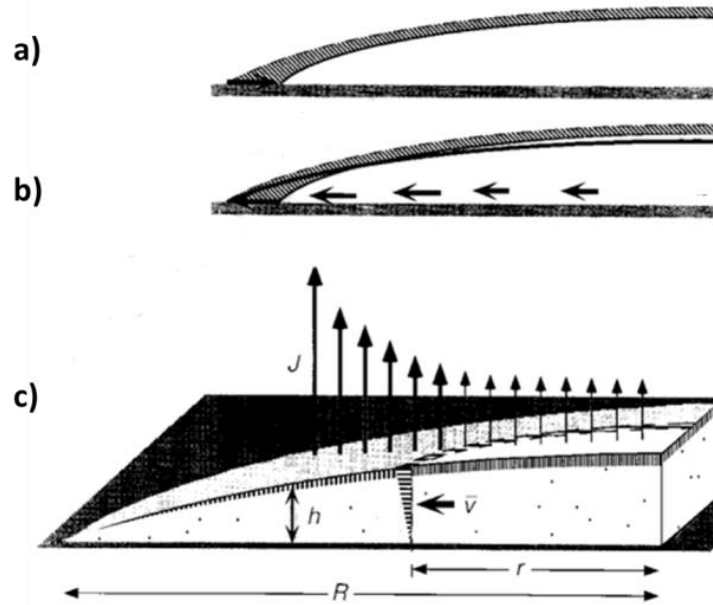


Figure 1.2 Schematic of Deegan's coffee-ring effect mechanism model: a) the droplet shrinks without inducing radial flow; b) the compensating flow makes up for pinned contact line; c) evaporation rate varied at different distance to the center of the droplet (for detailed discussion see *section 1.2*)^[24]

As initial attempt for evaporation induced self-assembly, patterns formed from evaporating a sessile droplet that contains nonvolatile solute on a solid substrate was closely studied^[28]. However, the resulting structures are usually too dissipative and irregular (Fig. 1.2) to reach the standard of applications such as data storage devices and microelectronics, where large scale highly ordered spatial patterns are desired^[29-31]. In other words, the evaporation process in this case is not fully controlled.

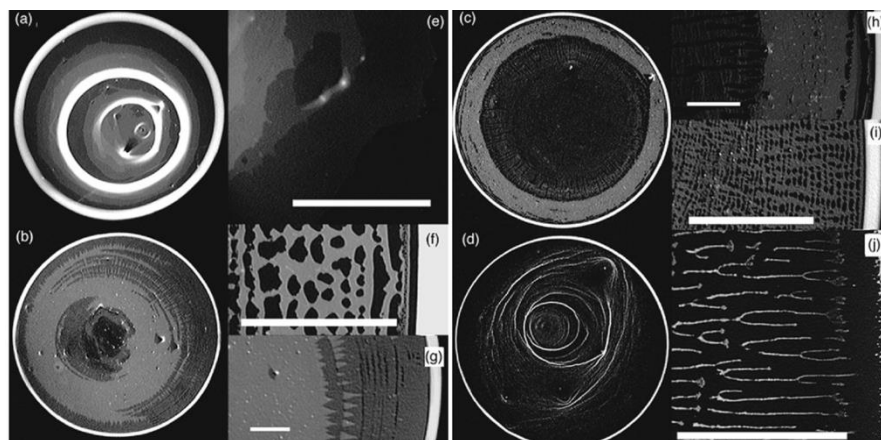


Figure 1.3 Photographs of deposit from evaporating drops of $0.1\mu\text{m}$ microsphere suspension at various concentrations. The left column shows the entire deposit for initial volume fractions: a) 1%, b) 0.25%, c), 0.13%, and d) 0.063%. The diameter of these drops is approximately 6 mm. The right column shows a close-up of the edge of the ring after evaporation process.^[28]

Further studies of the external flux inside the droplet during evaporation indicate that many factors can strongly influence the final deposited pattern, such as evaporation flux, radial flow, Marangoni flow and interactions between substrate and solutes (see **Section 1.2** for specified discussion). To date, many impressive studies have been focused on developing techniques to deliberately control the evaporation for rapid and cost effective surface patterning by manipulating those factors. The basic idea behind those attempts is to introduce confinement to the evaporating surface and restrict the solution. The restrictions include two parallel sliding glass substrates^[32, 33], “curve-on-flat” geometries^[34-36], and cylindrical tube^[21, 22].

As an example, controlled evaporative self-assembly (CESA) is a simple yet effective geometric restricted method to craft large-scale periodic structures (Fig.1.3). The solution is confined in the gap between the upper curved surface and flat substrate (i.e. “curved-on-flat” geometry) by capillary force, so the evaporation can only happen at the capillary edge where the evaporation rate reaches its maximum since it’s the contact line(similar to coffee-ring situation). With the evaporation process ongoing, the volume of

solution shrinks and the contact edge gradually jumps inward, which leave behind concentric rings constructed by the solutes (polymer^[3, 22], quantum dots^[35], carbon nanotubes^[37] etc.). More precise controlling over the evaporating process can even lead to additional secondary structure like pinholes^[36]. However in this system too many parameters (concentration, confined height, contact line moving speed etc.) are changing coherently and they are difficult to be controlled in real-time and directly. The continuously changing parameters also lead to regular patterns with gradient change. Fig1-3 b) shows a clear decrease in center-to-center distance (λ_{c-c}) and pattern height between the concentric rings as the solution gradually dries up.

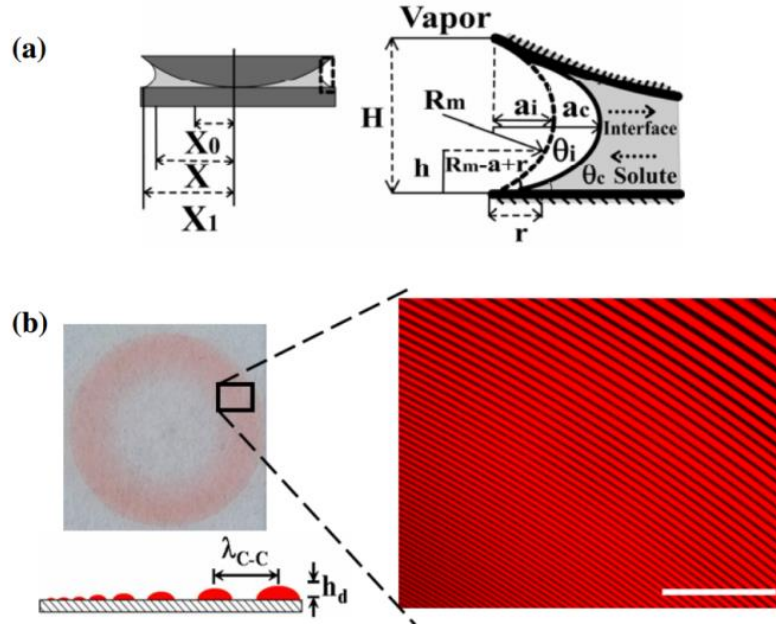


Figure 1.4 Typical curved-on-flat geometric restrictions, “sphere-on-flat” in particular. a) Schematic cross section view of a capillary-held solution (left) and close-up of the capillary edge during evaporation (right); b) A small zone of fluorescent image of MEH-PPV rings in red, scale bar=200nm.^[35]

Flow-enabled self-assembly, on the other hand, stands out to solve those problems while maintaining CESA’s advantages. In this method, two- plate confinement is applied

and the programmable motion of lower plate makes it possible for precisely controlling the evaporation flux and the interfacial interaction between the solute and substrate in real-time. Mechanism of why this precisely control happen will be supported by recent progress of theoretical study of evaporation process (*Section 1.2*), and applications and the details of FESA set up will be introduced in *Section 1.3 and 1.4* respectively.

1.2 Mechanism and Theoretical Model of “Coffee Ring” Effect

Knowing that the coffee-ring mechanism proposed by Deegan in 1997^[24] is a simplified model, a more accurate and detailed modification of Deegan’s model is desired to understand the nature of coffee-ring effect. Recent study of coffee-ring effect indicates that the formation of a deposited ring-like structure of non-volatile solution can be divided into four indispensable steps^[38]:

Step1. Flux generation

In this step, radial evaporation rate gradient at air-solvent interface of the droplet generates a capillary flow towards the contact line. Apparently this process exactly fits Deegan’s model.

The study of evaporation process of aerosol droplet system has been well developed over the past century^[39, 40]. A classic evaporation flux model of drying an aerosol droplet in air can be described by Hertz-Knudsen relation^[41]:

$$j = \alpha \sqrt{\frac{k_B T_s}{2\pi M_l}} \frac{\rho_s - \rho_v}{\rho_l} \quad \text{Eq.1-1}$$

where α is a material specified accommodation coefficient related to phase change. This equation can be simplified as follows in quasi-stationary and homogeneous temperature situation^[42]:

$$j = \frac{j_0}{R} \quad \text{Eq.1-2}$$

where R is droplet radius and $j_0 = D_m \frac{\rho_s - \rho_\infty}{\rho_L}$ is an evaporative parameter.

Equation1-2 and future study on case that a hemispherical droplet dries on substrate,^[43] indicating a clear consistency that the evaporation flux is directly related to the droplet size. Here, we focus on two important evaporation models based on this inspiration:

The lens evaporation model

Based on above equation Deegan deduced the following equation for droplets whose contact angle θ is less than 90° (the hydrophobic surface situation is a more complex system^[44] and will not be discussed in this thesis)^[24],

$$j(r) \propto (R - r)^{-\lambda} \quad \text{Eq.1-3}$$

where $\lambda = \frac{\pi - \theta}{2\pi - \theta}$, R and r are geometric parameters of the droplet defined in Fig.1.2

c. Note this relationship can be reduced to thin droplet when θ goes sufficiently small and thus λ will be ~ 0.5 . A better fit for thin droplet evaporation was proposed by Hu & Larson as follows^[45, 46]:

$$j(r) = \frac{J_{lens}}{(R^2 - r^2)^\lambda} \quad \text{Eq.1-4}$$

By assuming the surface of the droplet is a cap part of sphere(Fig1.5), one can substitute R and r as a function of h and d_0 ^[46]:

$$\frac{h}{d_0} = \sqrt{R^2 + d^2 - r^2} - d,$$

$$\text{where } d = (R^2 - d_0^2)/(2d_0)$$

Eq.1-5

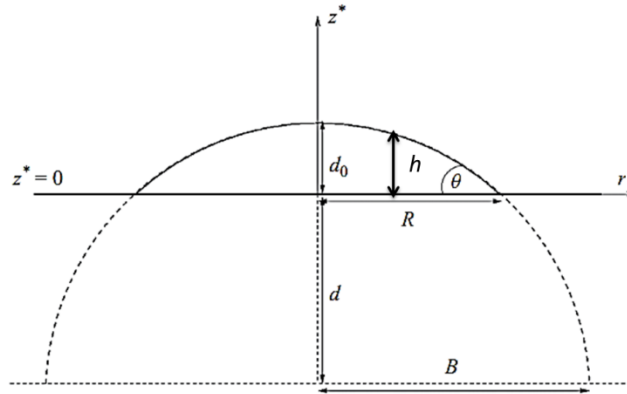


Figure 1.5 Schematic for spherical cap approximation^[46]. (The figure has been modified for notation self-consistency and h was added to the original figure.)

Merging h to the Eq1-4 and making the new equation dimensionless by $[J] = (k\Delta T)/(d_0 L)$, one can obtain the following equations^[46]:

$$j(h) = \frac{J_{lens}}{[J]d_0^{2\lambda} \left(h \left(\left(\frac{R}{d_0} \right)^2 - 1 + h \right)^\lambda \right)} \quad \text{Eq1-6}$$

For small contact angle situation (i.e. thin droplet, or at near contact line area), Eq1-6 can be further reduced to^[46]:

$$j(h) = \frac{\chi}{h^\psi} \quad \text{Eq1-7}$$

where under small contact angle assumption, $\psi = \lambda$. Note R and d_0 are treated as constant when the shape change of the drop goes slowly. Eq1-7 is also valid for large contact angle situation, with $\psi = 2\lambda$.^[46]

Eq1-7 represents the key message from lens model that the evaporation flux is inversely related to the local thickness of the droplet. In fact this model fits experimental results reasonably well, where r is small (i.e. near the center of the droplet). However at the contact line area ($h \sim 0$, $r \sim R$), j goes to infinity, which is physically incorrect.^[47]

The NEOS evaporation model

The NEOS model, abbreviated from Non-Equilibrium One-Sided, was initially brought up for a specific case where phase transition is negligible in evaporation process^[48] (i.e. “reaction-limited” evaporation^[46]). In this case, vapor phase has negligible influence to the evaporative flux and only liquid phase should be considered. The boundary condition for NEOS model is as follows:

$$j(h) = \frac{1}{h+K+W} \quad \text{Eq. 1-8}$$

where K and W represent non-equilibrium parameter and thermal effect respectively^[46]. This model was first applied to thin film evaporation by Burelbach et al^[49] and was further expended by Oron, Davis & Bankoff^[50]. Unlike in thin droplet where $h=h(r)$, thin film have uniform thickness (i.e. h) everywhere. With thin film assumption, given liquid species, film thickness and substrate thickness, K and W can be treated as constant, i.e. ^[46]

$$j(h) \sim \frac{1}{h+const} \quad \text{Eq. 1-9}$$

Comparing Eq. 1-9 with Eq.1-7, apparently at contact line where h goes to 0, evaporation flux in this model is finite. The difference of lens model and NEOS model is clearly evident in Fig.1.6

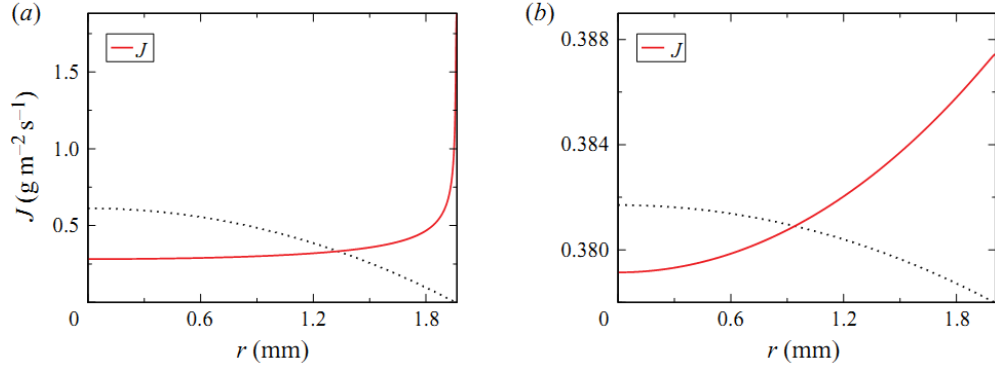


Figure 1.6 Numerical evaporation flux j versus radial coordinate r results of water drop calculated by a) Lens model; b) NEOS model. The dash lines are the corresponding drop profile.^[46]

Note that the above 2 models focused on the flux inside the droplet. The flux on the surface of the droplet, on the other hand, can hardly be measured until the past decade when digital holographic interferometry is well-developed and intensively used to characterize the global evaporation flux^[51,52]. The thick dotted line in Fig1.7 represents the experimental result of local evaporation flux of a droplet.

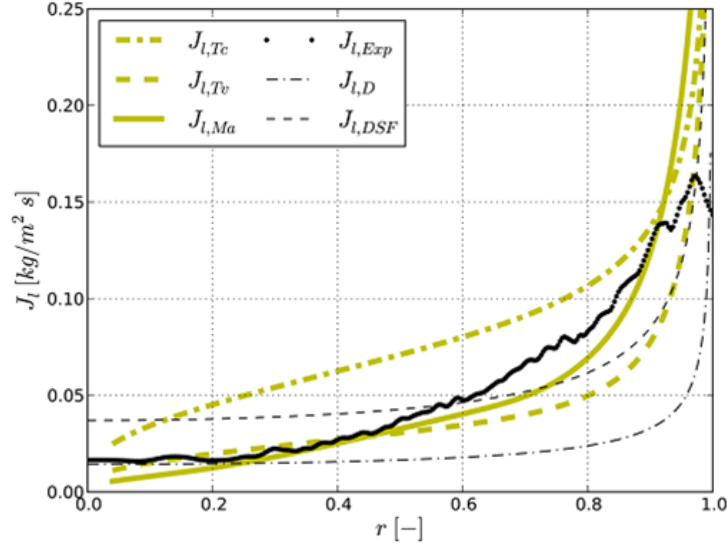


Figure 1.7 Local evaporation rate versus non-dimensionalized $r[-]$, which by notation of this thesis is equal to $\frac{r}{R}$, here $R=1.81\text{mm}$.^[51]

Note that in order to understand coffee ring effect we are focusing on the flux that can really carry the solute or suspended particles. To this end in Fig.1.7 we only concern the experimental result where $r[-] \sim 1$ (i.e. the surface flux near contact line.). As the flux doesn't significantly increase near the contact line area nor reach singular point at the contact line, this result serves as great evidence to support NEOS model at the contact line region.

Step2. Solute transportation

In this step the radial capillary flows effectively carry the nonvolatile solute to the contact line, resulting from the evaporation flux generated in step1. Dedicate study of the flow inside the droplet during evaporation indicates that there are two kinds of major flows functioning and favor to form entirely deferent patterns^[38]- one is radial flow, which is induced by evaporative flux at the contact line, and the other is Marangoni flow, which is

induced by surface tension . Unlike radial flow which carries the solute or suspension towards the contact line, Marangoni flow tries to bring them back to the top of the surface and position them at the bottom center of the droplet.

Radial Flow

First noticed by Deegan in 1997^[24], radial flows inside the evaporating droplet act as the main carrier for solute transportation to the contact line and get deposited. In other words, radial flow is essential for coffee ring formation. The amount of accumulated suspension at the contact line M is found to be both droplet size R and the evaporation time t , specifically^[24]:

$$M(R, t) \sim t^{1.37} \quad \text{Eq.1-10}$$

Based on Eq1-10 and Eq1-3, the velocity of the radial flow that transports the solute to the contact line at time t is:

$$v(r, t) = \frac{-1}{\rho_l r h} \int_0^r r \left(j(r) \sqrt{1 + \left(\frac{\partial h}{\partial r} \right)^2} + \rho_l \frac{\partial h}{\partial t} \right) dr \quad \text{Eq.1-11}$$

Similarly to what we have discussed in ***step1***, the velocity of the radial flow goes to infinity at contact line ($h \sim 0$), and that's where NEOS model applies. Indeed, the NEOS approximation was introduced by Fisher et al.^[53] and the evaporation flux (Eq1-3 as in lens model. Note this paper published before the work performed by Hu & Larson. So the modification was based on Deegan's model, rather than Hu & Larson's modification) was thus modified to be:

$$j(h) = \frac{1}{h+K} [1 - e^{-A(r-1)^2}] \quad \text{Eq.1-12}$$

The corresponding velocity of radial flow under sessile droplet assumption is^[53]:

$$v = -\frac{1}{Ca} \frac{\partial}{\partial r} \left[\frac{1}{r} \frac{\partial}{\partial r} \left(r \frac{\partial h}{\partial r} \right) \right] \left(\frac{1}{2} z^2 - hz \right) \quad \text{Eq.1-13}$$

where Ca is capillary number (this concept will be revisited in **Section 2** with more detailed discussion), z is vertical distance to the bottom of the droplet ($z_{max}(r) = h(r)$). According to the above equations, velocity field for a pinned or sessile droplet where the mass flux follows the rule as Eq1-12 is shown in Fig.1.8. It's also obvious that the trend of radial flow is from the center to the contact line. This trend is easy to understand since evaporation flux is higher when h is smaller (near contact line) according to Eq.1-12, and thus induces a capillary force to generate the radial flow. Even more accurate model can be obtained when the convection and diffusion inside the droplet are considered^[47].

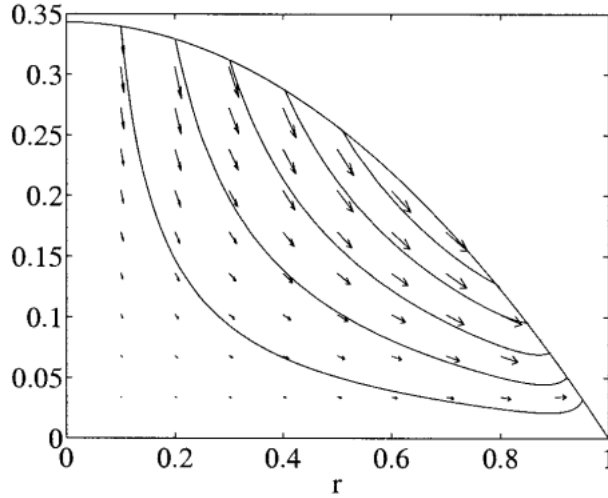


Figure1.8 Representative velocity vectors and streamlines for pinned droplet obtained from Eq.1-12 and 1-13^[53].

The maximum radial velocity, however, is reached at $r/R \sim 0.8$ rather than contact line (Fig 1.9 a), while the vertical component of the flow velocity has clearly directional

reversion from droplet center to contact line (Figure 1.9 b). Those experimental results indicate the radial flow is recirculating between the droplet center and edge.^[54]

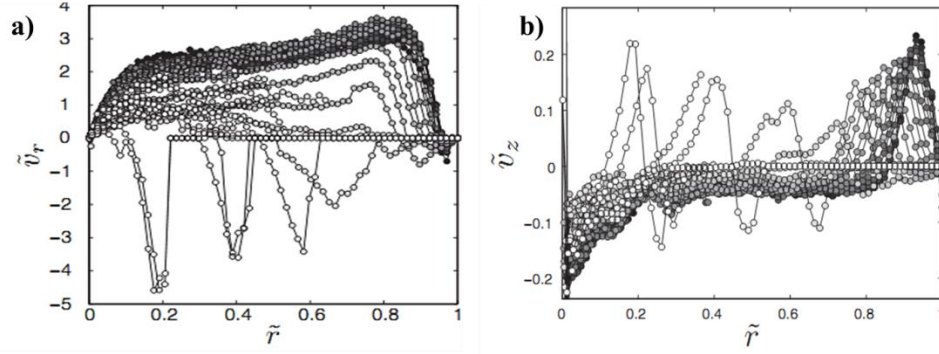


Figure 1.9 Radial a) and vertical b) component of the velocity of evaporative flux at different relative radial position (\tilde{r} in this figure has been normalized to dimensionless with the original droplet size R and total drying time) at $z = 10\mu m$. The dark dotted data points were taken at the beginning of the evaporation process, while the white dotted data points were taken later.^[54]

Marangoni Flow

Similarly to radial flow model which is inspired from coffee ring effect, the discovery of Marangoni flow actually comes from another interesting daily seen phenomenon: “tears of the wine”, or “legs of the wine”. Tears of the wine are commonly seen at the inner surface of a glass just above the inside wine (Figure 1.10 a). The whole process happened spontaneously and no pre-wetting on the inner surface of the bottle or perturbation (for example, shaking) to the bottle is needed. Long-term and close up observation indicate those tears are continuously generated and drop back to the wine. It seems like the wine is “running uphill”^[55], while the “driving force” to this unusual motion is actually induced by surface tension gradient^[56].

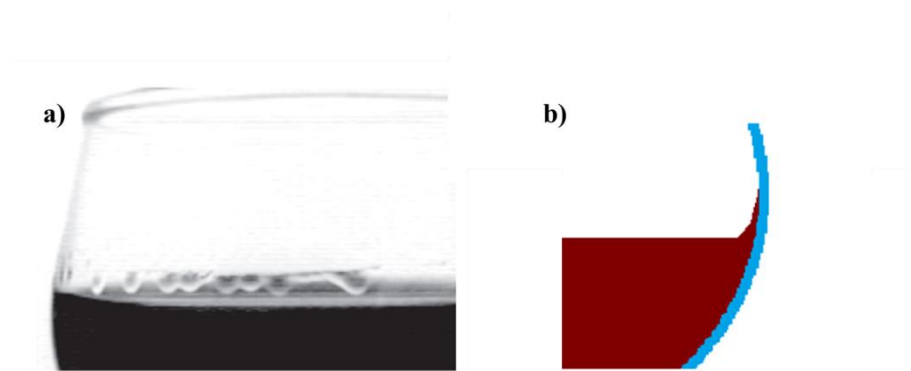


Figure 1.10 “Tears of wine”: a) Digital photo of bottle filled with mixture of water and commercial ethanol. Tears of wine are clearly shown on the bottle surface within minutes without agitation needed^[57]. b) Schematic of close up wine-vapor interface.

In the case of wine, which is basically a mixture of water and alcohol (ethanol), ethanol is much easier to evaporate (i.e. more volatile) while the surface tension is lower compared with water. So at the liquid-vapor interface the concentration of ethanol is lower than the main part of the wine, and thus higher surface tension than the main part is generated. This surface tension gradient is continuously dragging liquids up to a certain height along the inner surface of the bottle (Fig 1.10 b) and stays there, until the gravity force pulls them back. This phenomenon is known as “Marangoni effect”, and the flow generated from surface tension is termed “Marangoni flow”^[58]. Aside from adding low surface tension volatile component to the liquid phase (concentration gradient induced surface tension gradient), this effect can also be achieved by introducing temperature gradient along the liquid surface^[56]. One way to produce temperature gradient is having nonuniform evaporation flux in the droplet (e.g. ethanol, methanol, and acetone) ^[59-61]. Detailed theoretical studies, about how temperature gradient can generate surface tension gradient and the critical surface tension above which viscous forces can be overcome and instability (flow) can happen has been discussed by Pearson^[62] and Nield^[63]. However their model didn’t fit experimental results in volatile liquid system^[64], and more precise results of real-time temperature distribution at the contact line and top of the droplet are needed^[65].

A useful parameter above which Marangoni flow can be induced is Marangoni number Ma ^[66, 67].

$$Ma = \frac{\Delta\gamma L}{\eta D} \quad \text{Eq.1-14}$$

where L is the size of the system and D is solvent diffusion coefficient. Although not shown in this equation, contact angle also serves as an important factor for the formation of Marangoni flow^[68].

Marangoni flow in an evaporating droplet can be observed and recorded by the motion of fluorescence nano-particles or tracer. As shown in Fig 1.11, the circular Marangoni flow is reversing radial flow, which carries the solute near the liquid surface back to the center of the droplet, plunges them down and flow back to the liquid surface for a new round of transportation^[69].

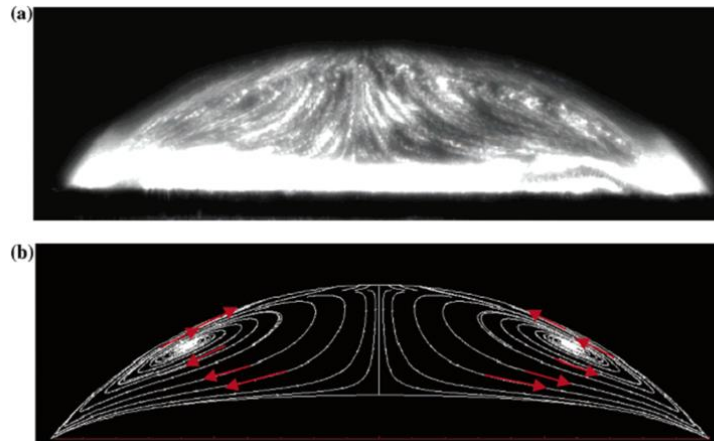


Figure 1.11 Flow field images a) taken from experiment and b) from theoretical prediction of evaporating octane droplet. Droplet in a) was not symmetrically illuminated for better objection of the vortex^[69]

Step3. Pinning process

In this step, the solutes get deposited along the contact line and form a strip. In this stage the droplet can be treated as a sessile droplet and it's in "pinning process", meaning the contact line is temporally immovable. Note that although contact line is pinned, the evaporation process continues and the volume of the droplet will shrink due to the mass loss of solvent. The key parameter that is changing during this step is actually contact angle θ , and it will continuously decrease with the volume shrinkage.

Besides, it's worth noting that the pinning process can also be strongly influenced by the interaction between the substrate and the solute^[38], even in the situation when Marangoni flows are negligible. In other words, in order to get the solute successfully deposited at the contact line, it requires strong interaction between the substrate and the solute. It is straight forward that if the solute and substrate strongly repulse each other (i.e. Hamaker constant < 0), the solute will never be deposited on the contact line, nor will they further induce coffee ring structure. On the other hand, however, if the solute and substrate have too much attraction with each other, the flow cannot afford to transport the solute and thus yield a uniformly deposited disk^[70].

Recent study has also shown the shape of the suspended particles can be a key factor^[71]. As shown in Fig 1.12, when drying droplets have the concentration, the one contains spherical particles successfully maintained a coffee-ring pattern, with the particles gathered, close-packed and deposited at the contact line. In contrast, the droplet contains ellipse-shaped particles left behind a monolayer colloidal film. The anisotropic shape of ellipse particles produced large surface viscosity (i.e. stronger inter-particle attraction) and thus strongly deformed interface^[72]. This mechanism is further proven by the restoring of coffee ring effect adding surfactant (SDS) to the ellipse suspension to lower the surface tension and thus reduce interface deformation (Fig 1.12 c). The surface viscosity of suspended particles can also be modified by particle surface modification^[73].

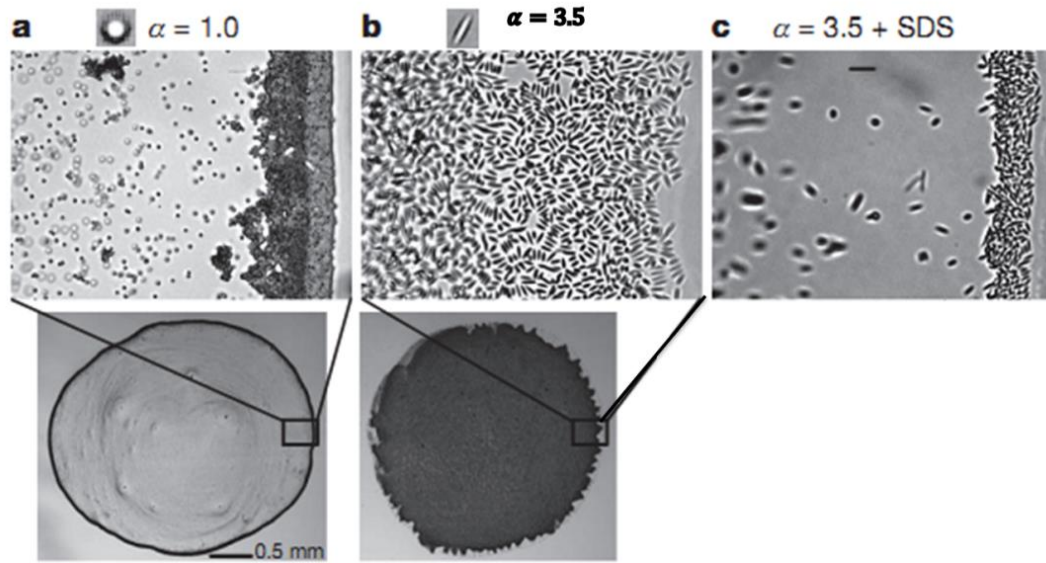


Figure 1.12 Patterns formed after evaporation of suspensions with different shape and close-up images of the particles near the contact line: a) Spherical shaped suspension b) ellipse suspension; c) Adding SDS (0.2% by weight) to the ellipse suspension and coffee-ring effect was restored.^[71] (Note: necessary modification from the original figure and correction of a typo in b) have been made)

Step4. Depinning process

With the evaporation process ongoing, the solvent loss due to the evaporation process leads to the curvature of the droplet surface increasing, and thus increasing the surface tension. As described in step 3, the contact angle of droplet will continuously decrease until a critical value θ_c is reached. When $\theta < \theta_c$, the depinning force driven by surface tension will overcome the pinning force, so the contact line “jumps” inwards. That’s how “depinning process” happens. Note that this movement of contact line has little influence to the deposited pattern generated in step 3, thus the future pattern generated from the four steps noted above can be treated similarly yet independently.

Despite the mechanism behind depinning process is widely accepted, most of the theoretical studies of this process are still too general and at the qualitative stage^[38, 74]. One of the breakthroughs to uncover the nature of depinning process is reported by Li et al^[75]. It is known that the pinning force proportional to the width of the deposited rings, they demonstrate that precisely programming the width of deposited rings, the critical contact angle can change inversely. For instance, the depinning force (horizontal component of critical surface tension) increases with the increase of ring width.

1.3 Crafting highly Ordered Structure via Flow-Enabled Self-Assembly

As described in section 1.1, flow-enabled self-assembly (FESA) is an evaporative self-assembly strategy using 2-plates geometry. The idea of this set up was originally comes from “slot coating”^[38], which has been a popular coating technique for precise coating since 1960s^[76, 77]. As the substrate continuously moves forward, the coating material can be laid on the substrate through a feed slot in slot dies (Fig 1.13a). Later on, “flow coating” was invented. Different from slot coating, the polymer solution was pre-injected to gap between the blade and substrate, and the blade is programmed to pull against the substrate while the substrate is stationary (Fig 1.13 b). Since flow-coating was originally invented to fabricate large scale thin polymer film with uniform thickness^[78], the polymer solution used are usually high concentration. On the other hand, since the upper blade moves during the whole process, the motor system and mechanical construction of the equipment can be more complex and oscillation may be induced to the system. For application of fabricating polymer film, however, the above drawbacks won't have significant influence as they will have little influence on the behavior of the viscous polymer solution.

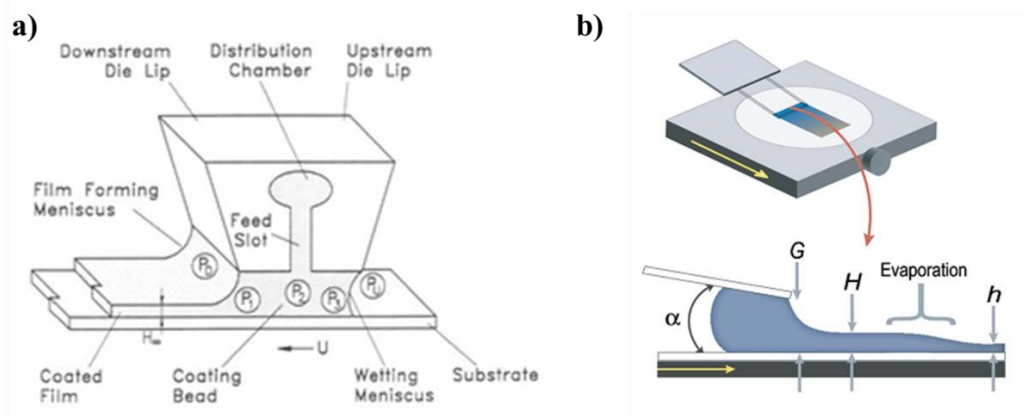


Figure 1.13 Schematic for a) Slot coating^[79] and b) flow coating^[78]

Interesting results were produced when the concentration of injected polymer solution is reduced. Since the concentration is low, the interaction between solutes is reduced and their behaviors are coupled to convections or other flux inside the solution. Instead of polymer film, convection-induced strips or spokes, dendroid patterns, honeycomb film etc. is generated on the substrate^[32, 80]. Most importantly, the idea of applying flow coating techniques to dilute solution shows promising potential in fabricating periodic micron-scale patterns over a large scale due to self-organization (or self-assembly) with the moving contact line^[32, 81].

Modified from flow coating, flow-enabled self-assembly (FESA) technique makes it easier and more straightforward to control every parameter that can influence the deposition of patterns with the guidance of mechanistic study of evaporative self-assembly (see section 1.4 for details about the set up and parameters). The most important distinction of FESA is that the movement of the contact line is controlled in programmable manner, thus the patterns periodicity is precisely tailored. This technique is lithographic-free 1D or 2D patterning method and has been extensively applied to generate intriguing patterns from various materials.

For example, using FESA technique, amphiphilic diblock copolymer Polystyrene-*block*-Poly (4-vinylpyridine) (PS-*b*-P4VP) assembled to micelles (Fig 1.14 a upper) and further constructed into micro-scale monolayer or double layer threads^[75](Fig1.14 b-e). The periodicity and thickness of the threads is controlled by adjusting the moving modes of the upper plate, and can be maintained even after centimeter-scale patterning^[75] (Fig1.14b). Those hierarchical patterns can also serve as templates to either directly assemble inorganic nano particles (lower panel of Fig 1.14 a)) or be nano-reactors encapsulated by precursors for further reactions^[38, 75].

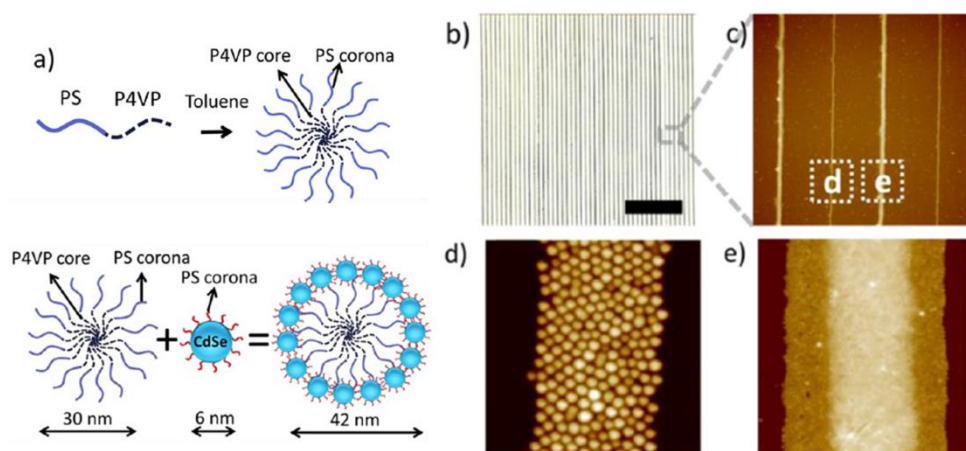


Figure 1.14 Crafting hierarchical structures of PS-*b*-P4VP micelles and threads using FESA technique: a) Schematic for formation of PS-*b*-P4VP micelles (upper) and how those micelles can serve as template to assemble inorganic nanoparticles (lower); b-e): Characterization of self-assembled threads: b) optical microscopic image c) AFM image at low magnification. d) AFM image of single layer thread. e) AFM image of double layer threads. Note the number of the layer is controlled by manipulating the stopping time in FESA process^[38, 75].

Another great idea to demonstrate the advantages of FESA technique is to align DNA nanowires over a large scale^[82]. By carefully tailoring the concentration and pH of the DNA solution^[83], moving speed of the lower plate and substrate temperature, ultra-long DNA arrays of high density and periodicity can be crafted. After transferring the crafted DNA arrays to desired substrate (Si) by swelling-induced transfer printing (SIT printing),

metal salts can be loaded to the substrate and absorbed by DNA, and large scale periodic metal nanowires array can then be obtained after plasma treatment.^[38, 82]

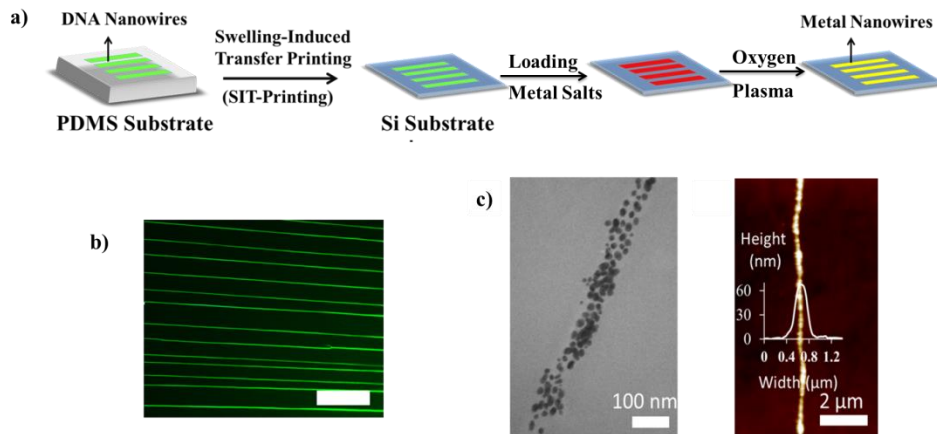


Figure 1.15 Macroscopic high aligned ultra-long DNA nanowires via FESA technique and its convections into metal nanowires: a) schematic for SIT printing and metallization of DNA nanowires. b) Fluorescence micrograph of continuous ultra-long DNA nanowires arrays crafted by FESA. c) TEM (left) and AFM (right) image of one assembled Au nanowire templated from aligned DNA nanowire.^[38, 82]

To summarize, flow-enabled self-assembly is a novel evaporation-induced self-assembly strategy and can be applied to pattern various kinds of materials into intriguing structures. Attempts of applying this technique to more materials will be introduced in *Section 3*.

1.4 System Setup of Flow-Enabled Self-Assembly

Schematic of the key operational portions of flow-enabled self-assembly (FESA) setup are shown in Fig 1.16.

As described above, the idea of two-plate geometry as configuration for evaporative self-assembly has been applied. The two plates (upper plate and lower plate) were nearly

parallel to each other with a constant and small intersection angle and a small gap (usually 3 to 5 mm) was formed where the injected solution goes in. The lower plate, which normally is the substrate to be deposited with patterns, is fixed on a moving stage. The motion of the moving stage is directly controlled in a real-time and programmable manner, and the substrate moves exactly in the same mode.

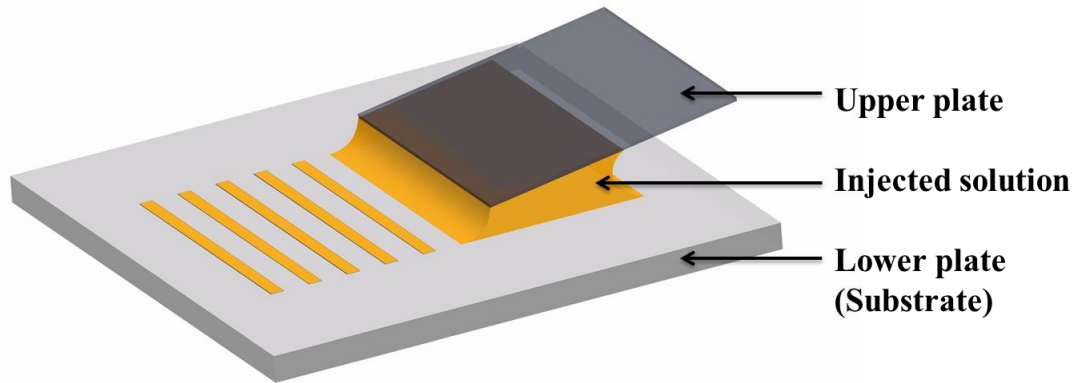


Figure1.16 Schematic for key parts of flow-enabled self-assembly (FESA) setup

The upper plate we used is half-cut micro cover-glass prepared prior to experiments. The upper plate can strongly influence to the final patterns if its relative position is adjusted. Before each round of injection, a new upper plate is mounted on an adjustable stage on an inverted U shape scaffold, which stands still above the moving stage. The adjustable stage has only 1 degree of freedom, which is the vertical rising or falling, and its moving distance is precisely measured by a micrometer caliper (degree of accuracy is 0.01mm). By setting up the position where the frontier of the upper plate touches the lower plate as origin, one can easily control the gap between the upper and lower plates. Note that the intersection angle between the upper and lower plate can be slightly tuned on the scaffold, and it indeed influences the flow behavior to some degree, although it will not be discussed in this thesis since it was kept constant in the following experiments. On the other hand, one should

always be careful in fastening the upper plate to the stage. Loosely placed upper plate can be partially, even totally, fall from the stage due to capillary force between the upper plate and the injected solution, which significantly intersects the angle and gap in an uncontrollable way and screws up the final result. Too tightly fastened upper plate, however, will make it difficult for upper plate replacement.

The whole FESA setup is shown in Figure 1.17. The moving stage and upper plate scaffold are placed on the observation stage of Leica optical microscope (Fig 1.17 b), where the real-time patterning process can be observed in-situ and captured either as high resolution digital image or video with various magnifications (observation lens of 5X, 10X, 20X, 50X). Both the moving stage and the optical microscope are connected to a desktop computer (Fig 1.17 a) where the software of movement-controller and Leica image processor are installed. Furthermore, a substrate heating system (Fig 1.17c and d) can be very useful when the heating temperature is needed to be customized considering the material properties of the injected solution^[82] (for example, for situation when the solute of the injected solution have high boiling point, which evaporates really slow at room temperature^[38]). In this case, a heating plate with an embedded temperature sensor is placed between the moving stage and the substrate, after setting a proper temperature in the controller (black box in Fig 1.17 c), the current that is being applied by the power supplier will be automatically tuned to maintain a relatively stable temperature on the heating plate based on the feedback of the temperature sensor. Moreover, hygrometer and thermometer are also equipped in case for highly sensitive flow coating system. We indeed have difficulty in reproducing some of the results in rainy or winter days in practice, thus recording ambient temperature and humidity is very important, specifically when constant-temperature-humidity chamber is not available.

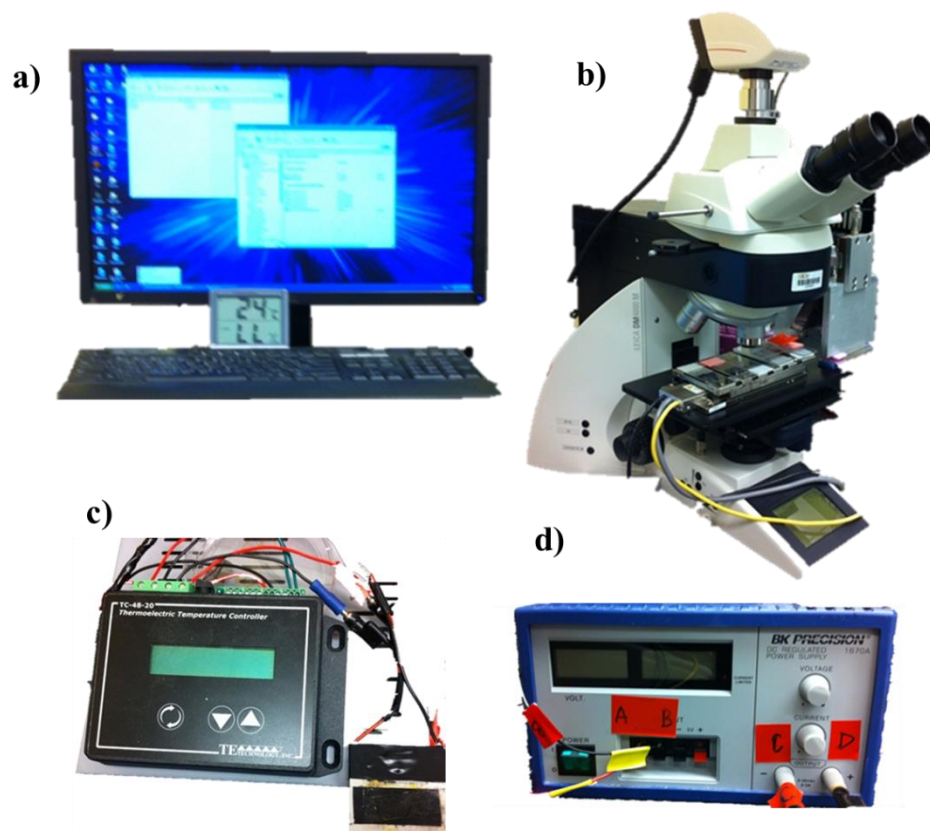


Figure 1.17 A complete setup for flow-enabled self-assembly: a) Desktop computer; b) optical microscope; c) and d): heating system including c) heating plate and sensor and d) temperature controlled power supplier.

1.5 Research Objectives

The objectives for this research are twofold: (1) Explore the mechanism of different deposited polymer patterns generated from flow-enabled self-assembly (FESA). In particular, polystyrene (PS) of different molecular weight in toluene solution was selected as a model system to elucidate how the solution properties influence the final FESA patterns. (2) Apply the mechanism from previous theoretical study and experiment to demonstrate the applications of FESA technique.

CHAPTER 2

MECHANISM STUDY OF POLYSTYRENE PATTERNS CRAFTED BY FLOW-ENABLED SELF-ASSEMBLY

2.1 Introduction

As one of evaporation-induced self-assembly strategies, the final pattern crafted via flow-enabled self-assembly (FESA) can be influenced by many factors, among which the extrinsic variables that can directly influence the evaporation process (for example, temperature, pressure, exposed surface area, etc.) are apparent and almost universal to all evaporation -induced self-assembly system^[21]. On the other hand, intrinsic variables also play important roles in tailoring the final patterns. The influence of solution concentration, solvent properties, compositions and molecular weight (note the weight average molecular weight will be used in this thesis) of solute have been systematically studied in previous research on controlled-evaporative self-assembly (CESA) for patterning polymers^[84].

Among all the internal variables, molecular weight (*MW*) can directly dictate the final patterns. The mechanism is that the solution with lower molecular weight solute will have low viscosity, and thus the pinning stage is shorter and weaker.^[84] Hong et al. has demonstrated various structures can be achieved using toluene solution of PS with different *MW* via CESA technique (as shown in Fig2.1):

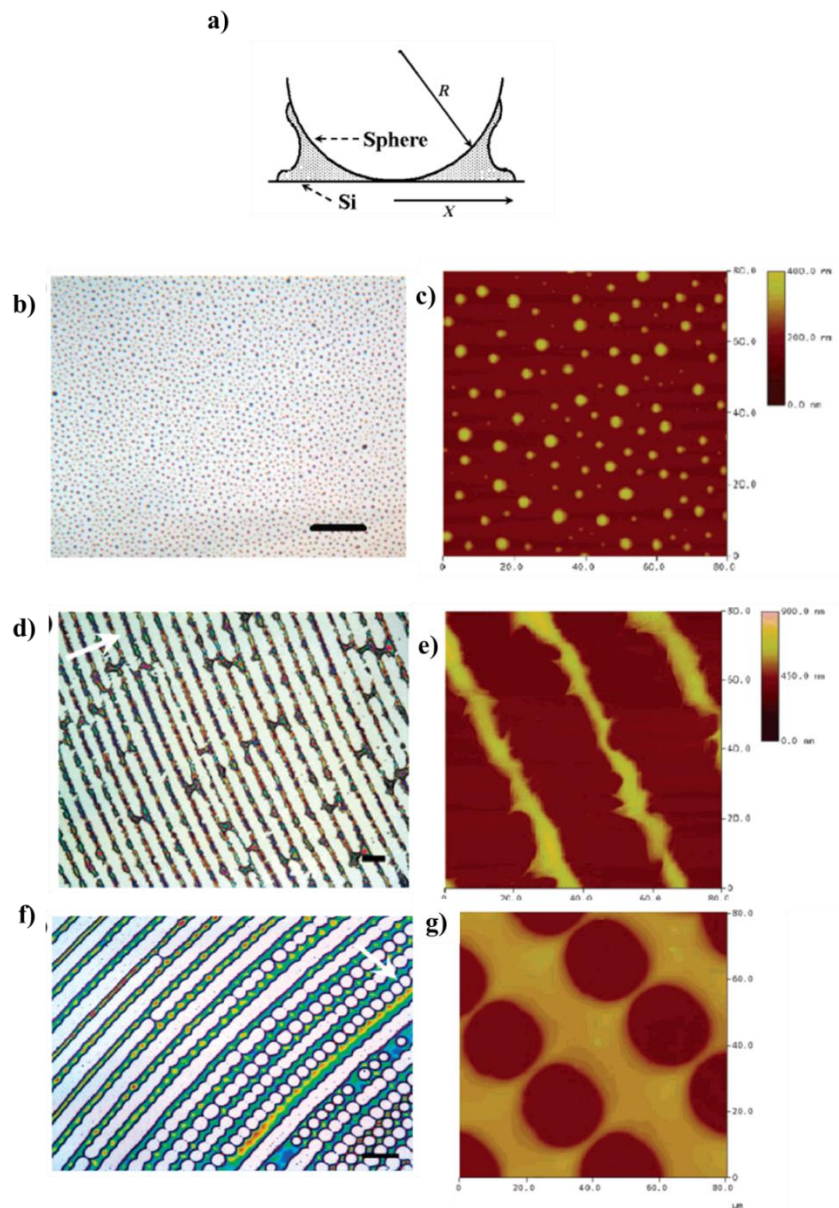


Figure 2.1 Schematic of CESA setup a), optical micrograph and AFM mapping of CESA pattern by: b-c) PS-60K; d-e) PS-112K; f-g) PS-420K in toluene. Concentration c is 0.25mg/mL. Scale bar = 70 μ m.^[85]

As shown in Fig 2.1, randomly dispersed dots, concentric ring patterns and punch-hole like structure have been generated by varying molecular weight of PS. At low MW, the dewetting process dominates so dots are generated. With MW increasing, coffee ring pattern, which in this case the concentric rings, are formed. At relatively high concentration,

punch-hole structure appears in addition to ring like structures. This phenomenon was explained by considering the evaporation velocity at the liquid front. Since the viscosity increase faster for higher MW PS solution^[86], fingering instability starts to play a role^[87] and finally leads to punch-hole structure.^[85]

Similar to the molecular weight effect, the solution concentration c can also affect the final self-assembled structure due to its influence to viscosity. In CESA case, however, the concentration effect is actually coupled with moving speed of the contact line. Xu et al., reported that lower solution concentration will lead to less deposition at the contact line and thus weaker dipping force, leading to more frequent depinning process and smaller strip spacing (λ_{c-c}) in CESA system.^[34, 35] Although it was pointed out that the decreasing of λ_{c-c} is due to lower moving speed of contact line v , the speed is failed to be characterized as the evaporation process of CESA cannot be controlled in real-time. The fact that both solute and solvent are lost during the evaporation makes it difficult to construct a sophisticated model for the evaporation process in CESA and decouple the effect from concentration and moving speed of contact line. Furthermore, intriguing structures can be induced at low concentration by enhancing fingering instability, dewetting or other mechanism^[32]. Other tricks to get intriguing complex structures are to use mixed solvent and composition (for example, diblock copolymers)^[88].

Similar phenomenon has been reported in many other self-assembly system aside from CESA system. One example is Langmuir–Blodgett patterning of phospholipid micro-stripes^[89], in particular, L- α -dipalmitoylphosphatidylcholine(DPPC) (the molecular structure is shown in Fig 2.2 g). Similar to dip-coating, the self-assembled patterns in Langmuir-Blodgett patterning system at gas-liquid interface can be transferred to a substrate which slowly moves out of the solution trough. A sensor is dipped in the trough and helps to maintain a constant surface pressure at gas-liquid interface. Langmuir-Blodgett patterning techniques is extremely suitable for amphiphilic polymers, and since the surface pressure is kept the same, the concentration is considered as constant (note in

this system the concentration is actually mass per unit area because the self-assembly only happens at the air/liquid interface and further forming monolayer). To this end, the effects of contact line moving speed (roughly replaced by the moving speed of substrate) and concentration (represented by surface pressure) are perfectly decoupled. Chi et al reported a significant effect of surface pressure and transfer velocity to the final self-assembly patterns^[89]. As shown in Fig 2.2, at lower transfer velocity, the self-assembled strip is perpendicular to the moving direction of substrate (i.e., parallel to the contact line, similar as coffee ring. See Fig 2.2 a) and d), while a higher transfer velocity will result in strips horizontal to the moving direction (i.e. perpendicular to the contact line, similar to fingering instability. See Fig 2.2 c and f). An intermediate velocity has also been observed, an in this case a grid structure (parallel and horizontal structures overlap) is formed (see Fig 2.2 b) and e)).

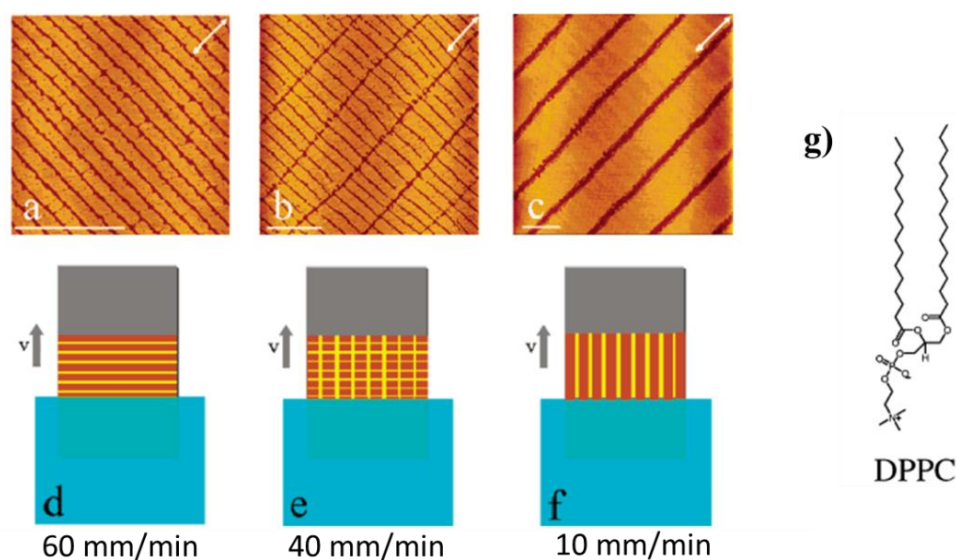


Figure 2.2 Patterns transformation depending on different moving speed of the substrate: (a-c) AFM images of DPPC patterns on mica surface at a) 60mm/min; b) 40mm/min; c) 10mm/min. The surface pressure in each case is 3mN/m. The double arrows in (a-c) indicate the moving direction of substrate; (d-f): Schematics of the formation of different Langmuir-Blodgett patterns corresponding to (a-c). g) Molecular structure of L- α -dipalmitoylphosphatidylcholine (DPPC) ^[89]

Furthermore, a phase diagram that illustrates the influence from both surface pressure and transfer velocity and their coherent effect has been obtained as shown in Fig 2.3 a). Aside from the pattern geometry, the spacing of patterns is shown to decrease with increase of the surface pressure (Fig 2.2 b) and transfer velocity (Fig 2.2 c).^[89] Note that the dependence diagram is obtained in the “in terminate” to “horizontal strips” region, so the research on the spacing dependent factor is not suitable in the perpendicular pattern case that is shown in Fig 2.2 a) and d).

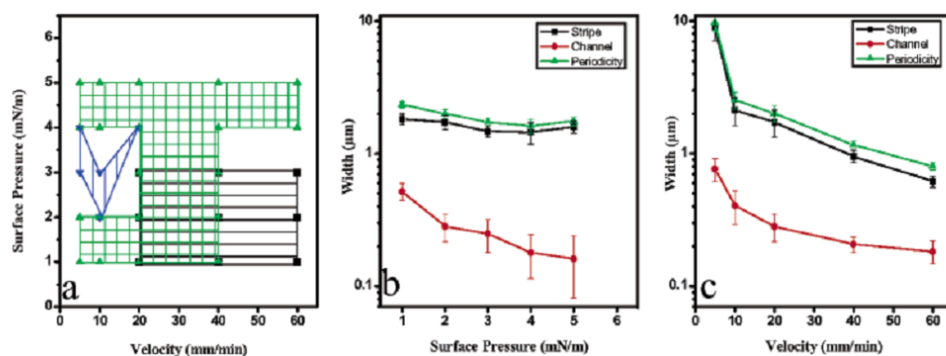


Figure 2.3 Qualitative analysis of effect of surface pressure and transfer velocity: a) Phase diagram of the stripe patterns on mica surface, in which horizontal stripes patterns is represented by black squares, grid pattern is represented by green triangles and vertical stripes is represented by blue triangles. (b-c) :width dependence of stripe (black), channel (red) and periodicity (green, refers to λ_{c-c} in the thesis) on surface pressure (b, at a constant transfer velocity of 20 mm/min) and transfer velocity (c, at a constant transfer surface pressure of 2 mN/m).^[89]

Although the influence of concentration and moving velocity of the substrate are successfully decoupled in Langmuir – Blodgett patterning technique, the pattern formation process, especially the self-assembly behavior at the three-phase contact line cannot be observed in situ^[89], and the size of possible patterning area is limited to the depth of LB trough. To this end, flow-enabled self-assembly (FESA) stands out as an excellent alternative that not directly controls the concentration and moving velocity of the substrate,

but also makes it possible for in-situ observation and extend the possible patterning areas to quarter size or even larger.

Herein, the effects of molecular weight (MW), initial concentration (c) and moving speed of the lower plate (v) on the final patterns are systematically studied by selecting poly-styrene (PS) toluene solution as a model system with continuous moving mode of FESA. Similar to the LB patterning of DPPD, 3 distinguishable patterns (strip, spoke, and their intermediate patterns) have been obtained, and the dependence of the spacing on the concentration and lower plate moving velocity has been scrutinized.

2.2 Results and Discussion

The pattern transformation in PS toluene solution was first detected by injecting small amount of solution (15 μ L) into the gap between the upper and lower plate, and use FESA set up to obtain the evaporative pattern at different evaporation stage until the solution dries out. Fig 2.4 shows 3 sets of optical micrographs taken at the beginning of the FESA process (the left row), during the process (the 2 middle rows) and at the end of the evaporation (the right row). Each set of the patterns comes from a continuous FESA process at a constant moving velocity of the low plate (0.001mm/s, 0.01mm/s and 0.1mm/s). Since the injection volume is too small comparing to standard requirement, and toluene is highly evaporative solute, the concentration of the solution is changing tremendously during the FESA process. PS with MW = 112K is used as solute and initial concentration of solution is 1g/L in all three sets of experiments. It's clear that at different evaporative stage of each set of experiment, the evaporation-induced pattern can be extremely different. To be more specific, when the lower plate velocity is 0.01 mm/s(Fig 2.4 b), the pattern generated at the beginning of FESA process is parallel to the lower moving direction (i.e., perpendicular to the contact line), which is denoted “spoke” pattern. With FESA process

going on, the spokes twist, break and contact in vertical direction and form a maze like structure, which is referred to “intermediate” pattern. When the solution is about to be totally evaporated, arrays of lines that are perpendicular to the moving direction (i.e. parallel to the contact line) starts to be formed, and is noted as “strip” pattern. Similar trend is found when the moving speed of lower plate is reduced to 0.001 mm/s (Fig 2.4 a), while the transition from spoke to stipe pattern is not completely finished since the pattern at the last stage of experiment is not perfectly periodic arrays of lines and still have pin-hole like structure, which would be treated as intermediate pattern. Interestingly, the pattern transformation trend becomes significantly different if the moving speed of lower plate is increased to 0.1 mm/s. Strips are generated at the early stage and gradually transformed to spoke patterns during the evaporation. When the solution is about to dry out, strip pattern is generated again.

Note for each set of experiment, the only variable here is the real-time concentration during the evaporation. With the deposition of PS on the substrate, the amount of solute decreases as well with the evaporation of toluene, so it's difficult to evaluate if the concentration increases or not in the FESA process (corresponding to the middle 2 rows of patterns in Fig2.4). However, since the solution concentration will go to infinite when the solution is about to dry out, it's obvious that the concentration at the last stage of the evaporation (corresponding to the right row in Fig 2.4) is larger than the initial stage (corresponding to the left row in Fig 2.4). Quick conclusion can be drawn from those experimental results, that is, at low concentration and low moving velocity of the low plate, spoke pattern will be generates. Otherwise strip pattern is preferred to be generated, with a possible intermediate stage in between. The experimental results also indicate that the concentration of the injected solution, moving speed of the lower plate, and molecular weight of PS solute are possible variables to determine the final pattern.

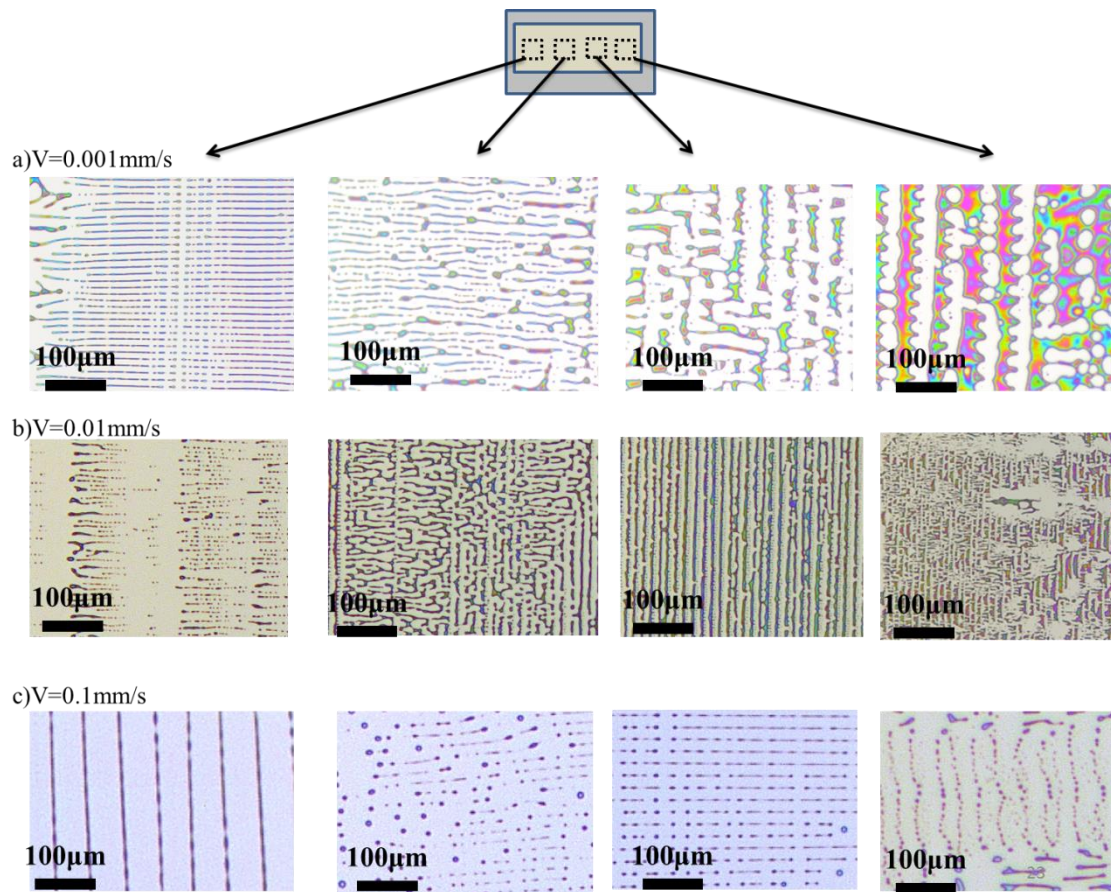


Figure 2.4 Schematic and optical micrographs of evaporation-induced patterns at different evaporative stage of 15 μ L PS toluene solution (left row: at the beginning of the evaporation; right row: at the end of the evaporation) and different lower plate moving velocity: a) 0.001 mm/s; b) 0.01 mm/s and c) 0.1 mm/s.

Systematic experiments on the influence of molecular weight (MW), moving velocity of lower plate v and initial concentration c on silicon wafer on the pattern formation have been conducted. One of the pattern collections is shown in Fig 2.5. When the moving velocity is less than 0.01 mm/s, spoke pattern is generated. When the moving velocity is between 0.02 mm/s and 0.07 mm/s, mash or pin-hole structure is formed, indicating an occurrence of transition. With the increasing of moving velocity, strip patterns are created, but disappear when the moving speed is too high. Although the final pattern created at $v = 0.001$ mm/s is dot-like arrays, in-situ observations indicate that it results from broken spokes due to dewetting, thus it should be classified as spoke pattern.

The results of pattern collections are summarized as phase diagram in Fig 2.6 and Fig 2.7. It is worth mentioning that although FESA technique has the capability of generating periodic patterns over large scale, the system we used here is highly evaporative and results in the change of real-time concentration. Thus, only the frontier pattern generated at the beginning of the FESA process are counted.

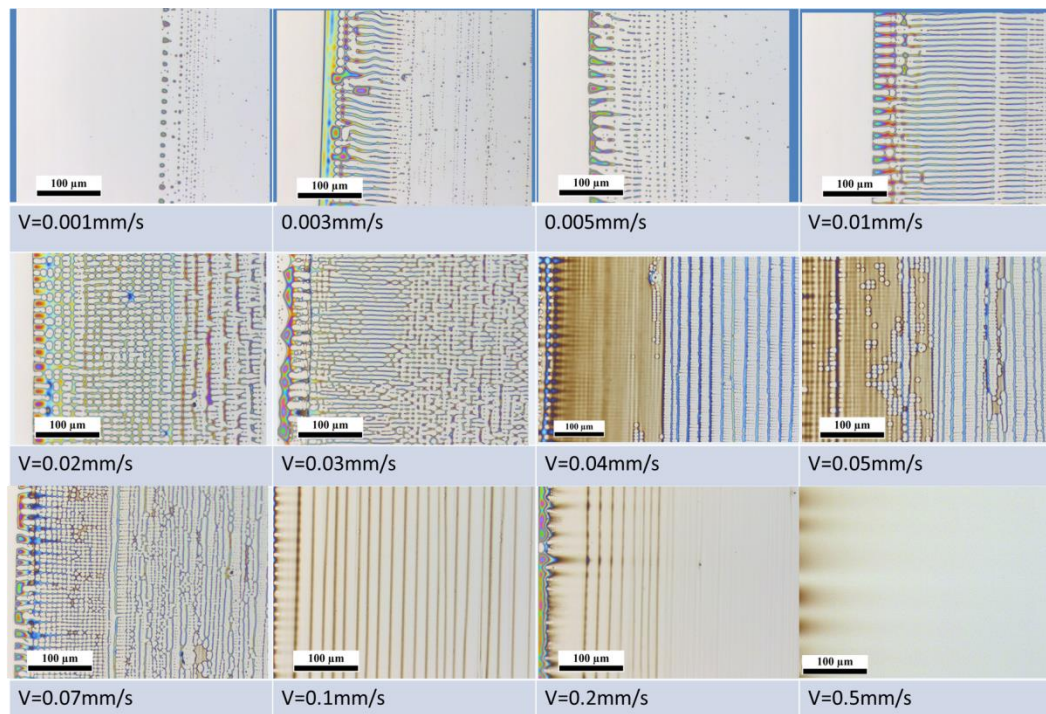


Figure 2.5 One of the collections of patterns created from FESA of 112 K-PS toluene solution at the concentration of 4.4g/L with different moving velocity v .

By keeping MW as constant (at 112K), Collections of Pattern of 112 K-PS toluene solutions at concentration of 1g/L, 2g/L, 4.4g/L, 8.7g/L have been summarized as 112K PS Phase Diagram in log-log scale shown in Fig 2.6, depicting data in multiple magnitudes of velocity and concentration. The data points are from experimental results, while the boundary of each region is estimated from the existing experiment results. According to the phase diagram, when MW of PS is constant at 112K, at low concentration and low

moving speed, spoke pattern is preferred to be generated, while higher moving speed leads to the formation of strip pattern. At extremely high concentration or speed, however, the film rather than the periodic arrays is generated due to the high viscosity or the low deposition rate. Despite the significant influence of lower plate moving velocity, the curved boundary also indicates the influence from initial concentration of the solution.

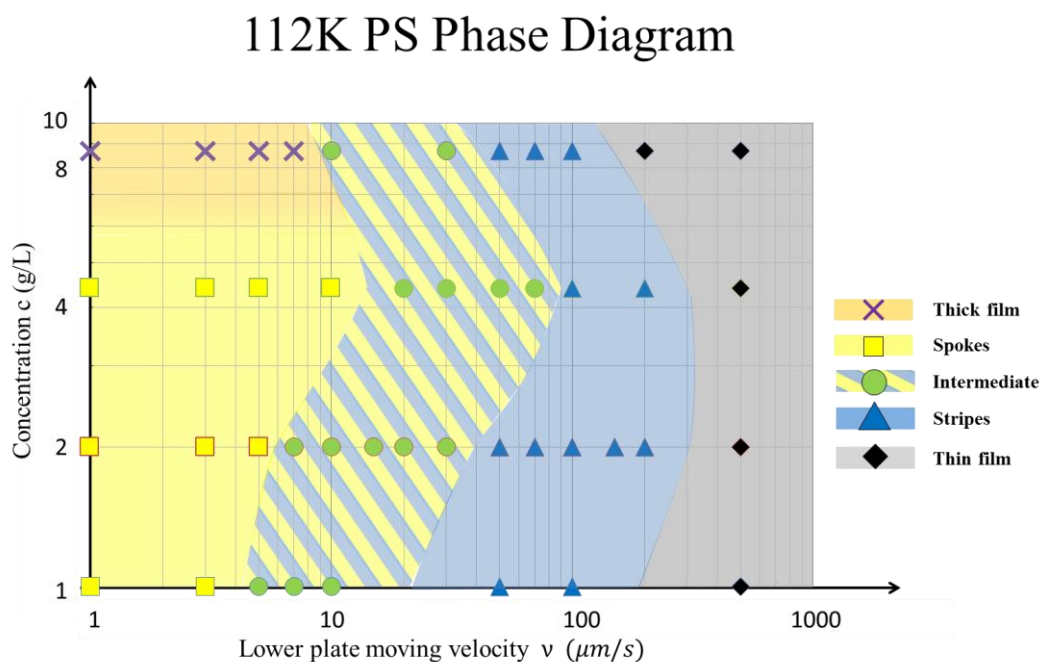


Figure 2.6 Phase diagram of 112K PS toluene solution on Si wafer depending on initial concentration and lower plate moving velocity according to optical microscopic observations. The phase diagram is composed of spoke pattern (yellow region with square data points), intermediate pattern (yellow/blue staggered region with spherical data points), strip pattern (blue region with triangle data points), thin film (gray region with diamond data points) and thick film (orange region with cross data points)

By keeping concentration constant (1g/L), patterns collections of 4.8k, 60K, 112k, 420K and 876K PS toluene solution have been summarized as 1M Solution Phase Diagram shown in Fig 2.7. Similar to 112-K PS Phase Diagram, log-log scale and same notation have been applied for self-consistency. Unlike 112-K PS phase diagram, dewetting becomes more severe in low MW samples such as 4.8k and 60K PS, which is denoted

“dewetted domains” at low v or dewetted thin film at high v . Interestingly, in 1M Solution Phase Diagram, the intermediate region is very narrow and even disappears together with the spoke pattern region when MW is too high (larger than 876K)

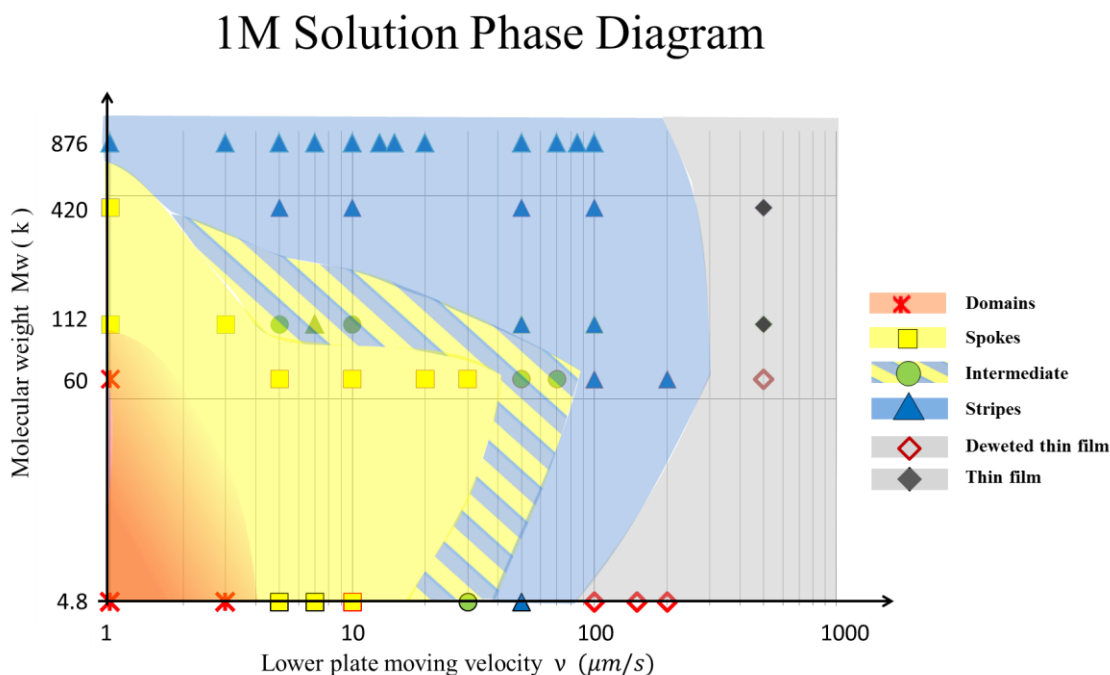


Figure 2.7 Phase diagram of 1g/L PS toluene solution on Si wafer depending on moving speed and molecular weight of PS according to optical microscopy observation. The phase diagram is composed of spoke pattern (yellow region with square data points), intermediate pattern (yellow/blue staggered region with spherical data points), strip pattern (blue region with triangle data points), thin film (gray region with diamond data points) and dewetted domains (red region with snowflake data points)

Comparing Fig 2.6 with Fig 2.7, it's clear that spoke pattern is usually generated at low moving speed v , low PS MW and low concentration c . In other words, the increase of these three parameters can hinder to the formation of spoke pattern. To elucidate why these parameters play important role in final pattern formation, the essence of spoke and strip patterns needs to be understood. According to chapter 1, it's obvious that the formation of strip pattern, which is perpendicular to the contact line, is resulted from coffee ring effect.

The spoke patterns, however, comes from a completely different mechanism, that is, fingering instability.

Fingering instability has been observed at the moving contact line driven by gravity or thermo-capillarity and extensively studied experimentally and theoretically since 1990s [87, 90][91-93]. A typical situation when fingering instability occurs is viscous current flows down from a slope^[94] (Fig 2.8), and the mechanism of the finger formation is instability of contact line resulted from Rayleigh instability^[87].

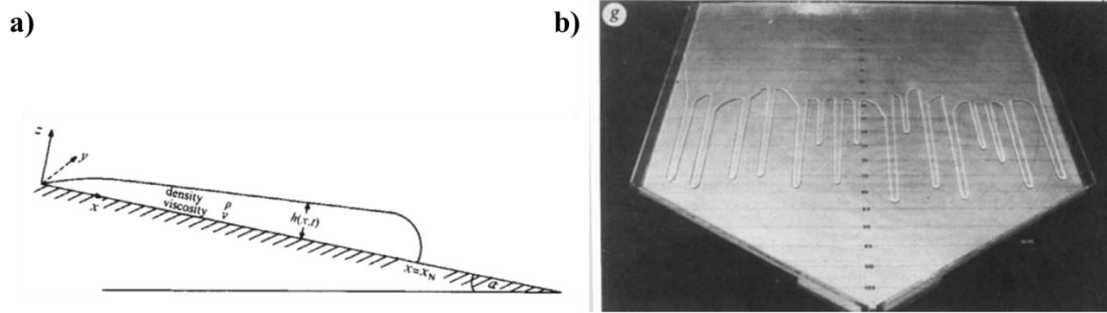


Figure 2.8 a) sketch and b) experimental result of the formation of fingering instability. Viscous flow is released on an inclined plane, and fingers are developed driven by gravity.^[94]

Theoretical study about fingering instability also shows that for fingering instability of Newtonian fluids, the finger width λ_f , is determined by Capillary number Ca ^[95, 96]:

$$\lambda_f \propto h(Ca)^{-\frac{1}{m}} \quad \text{Eq. 2-1}$$

$$\text{Where } Ca = \frac{\eta v}{\sigma} \quad \text{Eq.2-2}$$

In Eq. 2-1 and 2-2, h is the film thickness, η is the viscosity of the solution, v is the moving speed of the liquid front or contact line, σ is the surface tension across the surface,

and m is a constant larger than 1. Note that capillary number can be of different form if the fingering instability is driven by thermo-capillary effect^[96].

Eq. 2-1 also indicates the influence of the film thickness h on the finger width. This influence can be nonlinear in many situations^[97]. In FESA system, however, the film thickness is precisely controlled by the gap between the upper and lower plates, and has been set as a constant in each experiment. So the influence of the gap height is not considered in our system, and h is treated as constant in the following discussion.

Combining Eq.2-1 and 2-2, one can easily reach the following equation:

$$\lambda_f \propto \sqrt[m]{\frac{\sigma}{\mu v}}, \text{ where } m > 1 \quad \text{Eq.2-3}$$

Considering the setup of FESA technique, it's clear that the velocity of contact line in Eq.2-3 is equal to the moving speed of the lower plate. On the other hand, previous research on intrinsic viscosity of PS in toluene solution indicates that both MW and c are correlated with η , as shown in Fig2.9^[98-100]. Note that although the plot in Fig2.9 b) is conducted with 730K PS, the trend is correct over a large range of MW^[98]. Other parameters that can determine the viscosity of the solution such as shear rate $\dot{\gamma}$ ^[99] are not discussed in the simplified system in this thesis and was treated as constant. Besides, the interfacial surface tension σ is simplified as constant since it's a function of intrinsic property of PS and toluene^[38].

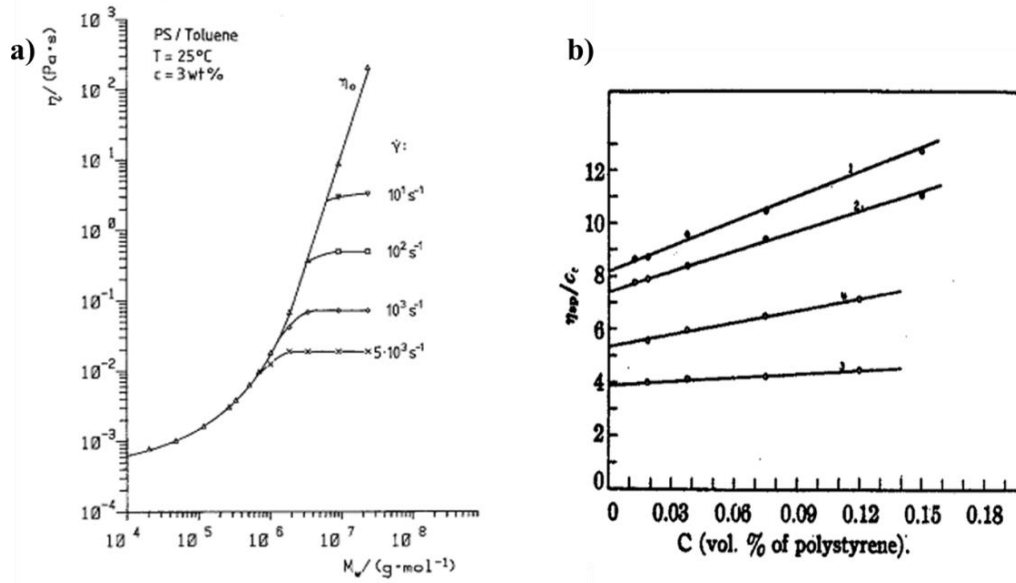


Figure 2.9 a) Molecular weight dependence^[98] and b) concentration dependence^[100] of intrinsic viscosity of PS toluene solution. The concentration of data in plot a) is 3wt%, and the MW of PS used for plot b) is 730K

Clearly, Eq.2-3 and relationship between MW, c and η predict a decrease of finger width with the increase of MW, c , and ν , and qualitatively agree with the experimental results. Fig 2.10 shows an example of relationship between the finger width versus the moving velocity of the lower plate, MW of PS and the solution concentration. The finger width approaches a minimum value with the increase of velocity and further increase of velocity will lead to pattern change from spoke to intermediate pattern. The channel width, which is the spacing between spokes, and pitch width, which is the center to center distance of the fingers (equal to the summation of the finger width and space width) also have a similar trend as finger width does with velocity.

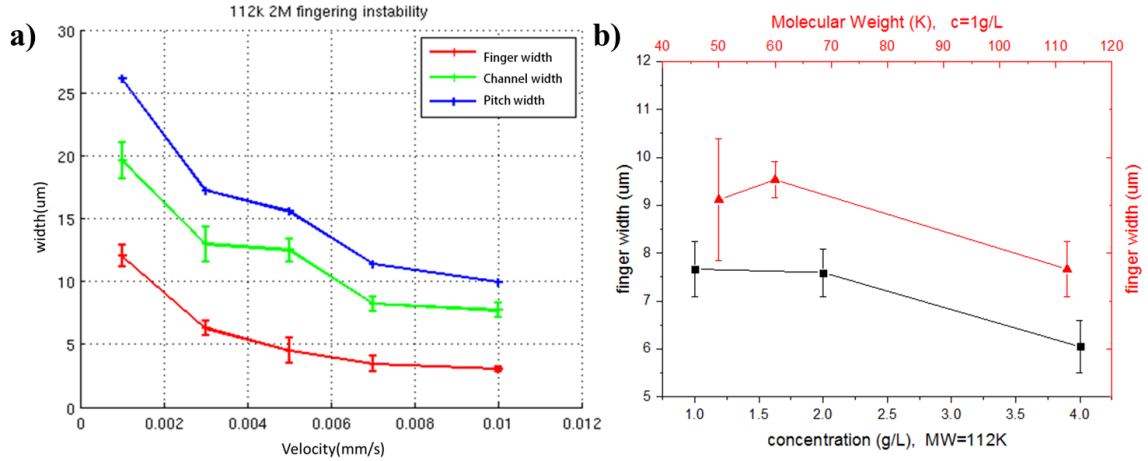


Figure 2.10 Relationship between the spacing of spokes generated from fingering instability and: a) the velocity of the lower plate (MW=112K, c=2g/L); b)-red, Molecular weight ($v=0.003\text{mm/s}$, $c = 1\text{g/L}$) and b)-black concentration (MW=112k, $v=0.003\text{mm/s}$).

Since the spoke pattern (perpendicular to the contact line) is formed due to fingering instability while strip pattern (parallel to the contact line) is formed due to coffee ring effect, the intermediate pattern is then easy to understand as a deadlock in the competition between fingering instability and coffee ring effect, and transition stage from fingering instability domination to coffee ring effect domination. A minimum finger width λ_{fmin} may exist below which distinguishable fingers cannot be formed and thus the transition from spoke pattern to strip pattern happens. On the other words, the perturbation of contact line (characterized by λ_f) should be large enough for the formation of fingers. Further experiments and theoretical studies are needed for this hypothesis.

In addition to the spacing of spoke patterns, the spacing of strips is also studied. 1g/L 876K PS toluene solution has been chosen for the spacing study because the system doesn't have spokes region or intermediate region at any possible velocity in FESA system (see Fig 2.7). Interestingly, although the strip width gradually decrease with the increase of the velocity, the pitch width and channel width decrease at the early stage yet increase later with the increase of velocity. Minimum pitch width and channel width and the corresponding velocity v_{min} are observed. Similar observation on the PS toluene solution

has also been reported in other evaporation-induced self-assembly systems^[32]. This “decrease then increase” trend of pitch width is caused by different moving mode of the injected solution during evaporation. When velocity of low plate $v < v_{min}$, the behavior of the solution will be similar to the sessile droplet model, meaning that the contact line will be pinned until the contact angle reaches its critical value. In this mode, the increase of lower plate moving velocity will decrease the pinning time in which solute deposition happens and thus decrease the width of the strip. When the velocity of the lower plate $v > v_{min}$, pendant moving will occur during FESA process. In this situation, since the moving speed of lower plate is too fast, after depinning, the contact line will slip for a certain distance before its get pinned again on the substrate. The slip distance increases with the increase of the moving velocity of the lower plate, so the channel width and thus pitch width will increase. This mechanism can be confirmed when comparing the velocity – width relationship of 4M and 8M 112K PS toluene strips pattern (Fig 2.12). The 4M plot shows exactly the same trend as Fig 2.11, while 8M plot only shows the sessile moving part (i.e., width decreases with the increase of velocity). The high concentration of 8M 112K PS toluene solution increases the viscosity of the system and avoids the occurrence of the pendant moving.

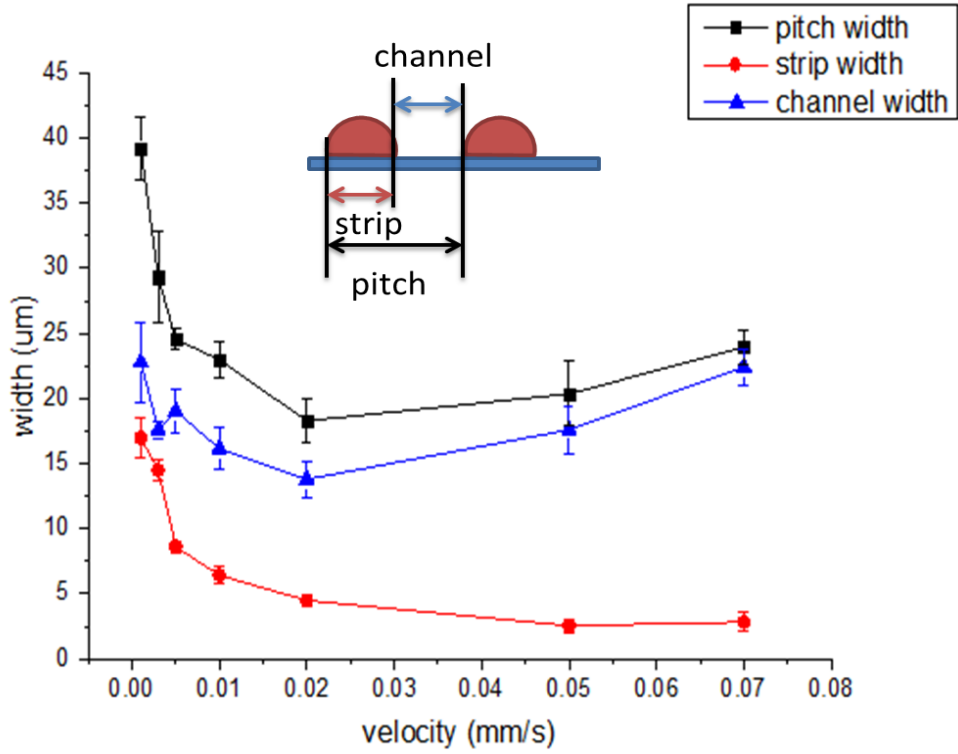


Figure 2.11 Relationship between the spacing of two adjacent strips and the velocity of the lower plate for 1M 876K PS toluene solution. The inset illustrates the pitch, channel and strip width.

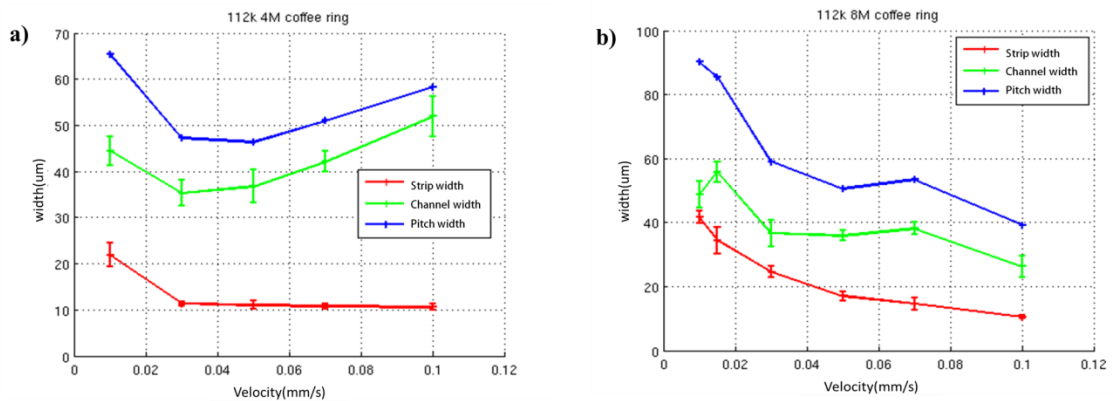


Figure 2.12 Relationship between the spacing of two adjacent strips and the velocity of the lower plate for the patterns formed from: a) 4M 112K PS toluene solution and b) 8M 112K PS toluene solution.

Similar trend that strip width decreases with increasing of velocity is broadly observed in many solution systems via FESA process. Specifically, the relationship between the PMMA strips and the moving velocity of the lower plate has been extensively studied both experimentally and theoretically^[38]. In previous work, Li et al. found that the width of PMMA strips crafted via FESA technique can be predicted using the following equation^[38]:

$$W_{strip} \propto \sqrt{\frac{8k_e D(1-H)C_v(A+BW_{stripe})}{v}} \quad \text{Eq. 2-4}$$

where k_e is the evaporation constant, D is the diffusivity of toluene, H is the relative humidity, C_v is the saturated vapor concentration of the toluene, and v is the moving velocity of the lower plate^[38]. The equation is simplified by assuming the cross section of the strip is half-circle. It turns out that the PS strips also fit Eq.2-4 (See Fig2.12 c). Besides, the pitch width, which is the center to center distance of adjacent strips, i.e., λ_{c-c} , is proportional to the strip width following the relationship in Eq. 2-5^[101]. The data fits both the relationships well in both PMMA and PS systems as shown in Fig 2.12:

$$\lambda_{c-c} \propto \frac{kW_{strip}}{\gamma \cos \theta} \quad \text{Eq.2-5}$$

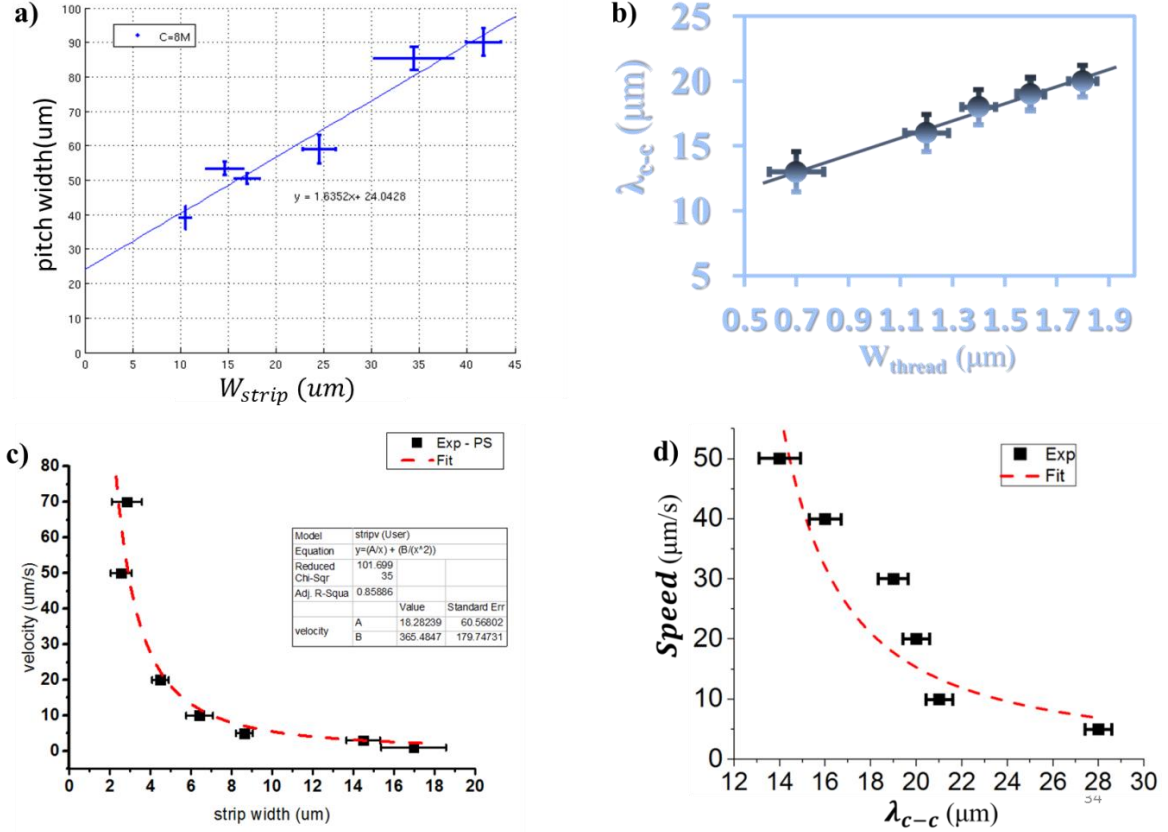


Figure 2.13 Relationship between the pitch width λ_{c-c} and strip width (W_{strip} or W_{thread}) for patterns formed (a, b) and the data fitting from Eq2.4 (c, d) from: a) and c) 1M 876K PS toluene solution; b) and d) PMMA toluene solution^[101].

2.3 Experimental

The Polystyrene (PS) polymers (Vender: Polymer Source Inc., Dorval, Montreal, Canada) used in the experiments were stored in refrigerator and used as purchase. 4.8K (Sample#: P4246-S, $M_n=4.8K$, $M_w=5.1K$, $M_w/M_n=1.07$), 60K (sample#: P4290-S, $M_n=60k$, $M_w=61.8K$, $M_w/M_n=1.03$), 112K (Sample#: P2915-S, $M_n=112K$, $M_w=118K$, $M_w/M_n=1.05$), 420K (Sample#: P4439-S, $M_n=420K$, $M_w=483K$, $M_w/M_n=1.15$), 876K (Sample#: P618S, $M_n=876K$, $M_w=1050K$, $M_w/M_n=1.19$) Polystyrene were used as solute

and toluene (Vendor: BDH, Radnor, PA, Cat No. BDH1151-4LG) was used as solvent. After adding a measured weight of PS polymers to a 10mL or 20mL volume of toluene, the polymer solution was sonicated in the valise for 15 min and stirred for 15 min by magnetic stirrer at room temperature to uniformly disperse the polystyrene in toluene. All of the solutions used in the experiments are freshly prepared, and were sonicated every 2 h.

4" (100)-oriented single crystalline Si wafers (resistivity = 0-100 ohm cm⁻¹) were purchased from Polishing Corporation of America, Santa Clara, CA, and were cut into 1*10 cm² for large-scale continuous patterning (experiment sets shown in Fig 2.4) and 1*2 cm² for regular FESA patterning by diamond knife as substrate. Prior to every single experiment, the Si substrate was washed with DI water and ethanol to remove possible dust and dried with high pressure Argon. After cleaning and drying, the substrate is then fastened on a computer-controlled motorized linear translational stage (Parker Hannifin Corp, mode: MX80LVixBL2b) using double-sided tape. The resolution of the translational stage is 100 nm, and the moving velocity can be set from 0.001 mm/s to 0.9 mm/s, with two motion modes for the translational stage. In the PS system study the continuous moving mode was used. In this mode the moving speed was set at a constant value with no intermittent stops in the process. The stop – and – move mode was used in *Section 3*, in which the moving velocity, the stop time as well as the distance of moving between each stop and the number of action rounds can be easily manipulated through programming.

The single-use upper plate used in the experiments were VWR micro cover glass cut in half (18X18mm as purchased and about 18*9mm after cut) prepared prior to the experiments. After setting up the lower plate (i.e. the substrate), the upper plate was partially mounted at an angle of 9.8° in a metal holder. The metal holder itself stands over the translation stage and remains motionless when the lower plate was moving. The back surface of the upper plate, which makes contact with the injected solution were blew with high pressure Ar to remove possible dust. Details about upper and lower plate set up can

be found in **Section 1.4**. 40uL PS toluene was pipetted to the gap between the upper and lower plate and then the translational stage was manually started to move right after the injection. At the end of each round of experiments, the sharp angle of a three-folded VWR light-duty tissue paper was squeezed into the gap to absorb and remove the redundant injected solution.

The in situ observation and optical micrographs were taken by Leica DM400M optical microscope (Serial No.: 0572794211) in bright field mode. Only the white balance was adjusted in the final optical micrographs and no further alterations were made to the micrographs. Selected morphologies of patterned polymer films (**Section 3.1**) were examined by atomic force microscope (AFM, Bruker Dimension Icon, Santa Barbara, CA; operated in the tapping mode at 0.5 Hz scanning rate). The tips used in AFM measurements were made by 0.01-0.025 Ohm-cm Antimony (n) doped Si with 50 ± 10 nm Al coated on the back side (Bruker, Camarillo, CA; model: TESPA; Cantilever: T: 3.5-4.5 μ m, L: 110-140 μ m, W: 25-35 μ m, f_c : 282-394 kHz, k: 20-80 N/m). All data analysis and figure plots were carried out using Microsoft-Excel 2010, OriginPro 9.1 and Matlab R2013b.

2.4 Conclusion

In summary, spokes resulted from fingering instability, strips as a result of coffee ring effect, and their intermediate patterns have been crafted from polystyrene toluene system via FESA process. The pattern transition indicates the competition of fingering instability and coffee ring effect inside the solution during evaporation. Systematic study of the relationship between molecular weight M_w , initial solution concentration c and velocity of lower plate v has proven that lower M_w , c and v are essential to the formation of spoke patterns, and a hypothesis of minimum finger width below which spoke patterns will not be formed is proposed base on experimental results and previous theoretical

studies. The relationship between the strip spacing and the velocity agrees with previous study on PMMA system, and the “decrease-then-increase” trend of pitch width (center-to-center distance of strips) is explained by switching between the sessile and the pendant moving of the contact line.

CHAPTER 3

APPLICATIONS OF FLOW-ENABLED SELF-ASSEMBLY

Y. Tao, C. Zhang, B. Li, Z. Lin, et al. “Facile Patterning of Donor-Acceptor Electrochromic Polymer via Flow-Enabled Self-Assembly”, (to be submitted)

L. Li, B. Li, C. Zhang, C. Tuan, Z. Lin and C. Wong, “A Facile and Low-Cost Route to High-Aspect-Ratio Microstructures on Silicon via a Judicious Combination of Flow-Enabled Self-Assembly and Metal-assisted Chemical Etching”, (to be submitted)

3.1 Introduction

As a bottom-up lithography-free approach, flow-enabled self-assembly of nonvolatile solutes by confined evaporation of volatile solvent is a simple yet robust technique to craft intriguing 0D, 1D and 2D structures on any desired substrates. Comparing to current conventional top-down lithographic approach such as e-beam lithography^[102], dip-pen nanolithography^[103] and photolithography^[104], the fact that FESA technique is extremely cost effective attracts even more interest for applications and potential commercialization. Specifically, large-scale periodic arrays of strips with controllable width and spacing are always desired in electronics^[105, 106], nanodevices^[107] and other applications. The strips pattern can be used either directly or indirectly. Despite patterning the desired material in target substrate, the patterns can also be used as mask to guide further surface treatment of substrate.

Herein, we demonstrate two examples of typical applications of flow-enabled self-assembly. In **Section 3.2**, facile patterning of functional donor-acceptor electrochromic polymers on flexible transparent substrate will be introduced as an example of direct use of FESA technique. In **Section 3.3**, applying strips crafted via FESA as mask to assist etching Si wafer for electronic and information storage will be detailed discussed as an example of indirect use of FESA technique.

3.2 Facile Patterning of Donor-Acceptor Electrochromic Polymer via Flow-Enabled Self-Assembly

Similar to “thermochromism” and “photochromism”, electrochromism describe the reversible change of a material’s optical properties (transmittance , reflectance, etc.) when external potential (i.e. voltage) are applied^[108]. It’s persistent yet reversible manner of color change makes electrochromic materials promising for applications in E-paper^[109], smart windows^[110, 111] and informational display^[112]. The underlying mechanism behind this property is electrochemically induced redox reaction^[113]. Among all conventional electrochromism materials, conjugated polymer clearly stands out as due to its straightforward band gap control and thus a rich variety of color changes by adjusting synthetic route^[114, 115]. Specifically, Donor-Acceptor (DA) approach, which contains both electron donor and acceptor along the conjugated backbone as repeated unit, expands the prospective of “color palette” of electrochromic conjugated polymers (ECPs)^[115, 116]. The dual-band absorption uniquely happened in DA polymer enhances the flexibility of manipulating color achieved by donor moieties control, and results in color-state such as green or transparent that used to be difficult to be achieved with π -conjugated polymers^[117, 118].

As discussed in *Section 3.1*, periodic patterning of ECPs is extremely important for its application in information display. Techniques that have been applied to pattern ECPs into micro or nano regime include photolithography and template assistant patterning^[119, 120]. Although high accuracy is achieved, the fact that extra photo-active units are needed to be incorporated into side chain of ECPs for UV radiation response leads to tedious extra synthesis^[120, 121]. Besides, carefully fabricated photo-proofed mask or exquisite template is needed, leading to complicated operation process and extra cost^[122]. Flow-enabled self-

assembly, on the other hand, provides a simple, cost effective and straightforward alternative for ECPs patterning. By understanding and utilizing the solution behavior during evaporation process, large-scale periodic ECPs strips can be crafted with no need of photo-active side chain modification, nor will any template be involved.

Herein, one of three donor monomers: indacenodithiophene (IDT), benzo [1, 2-b: 4, 5-b'] dithiophene (BDT) carbazole (Cz), and one of acceptor monomers of 2, 1, 3-benzothiadiazole (Tz) and Tz modified by 3-Hexylthiopene (HT) and/or thiophene (th) units are combined to synthesize novel donor-acceptor electrochromic conjugated polymers, among which Poly (Cz-HT-Tz), Poly(IDT-Tz) and Poly(IDT-HT-Tz) are successfully patterned via FESA approach. The chemical structures of those DA polymers are shown in Fig.3.1.

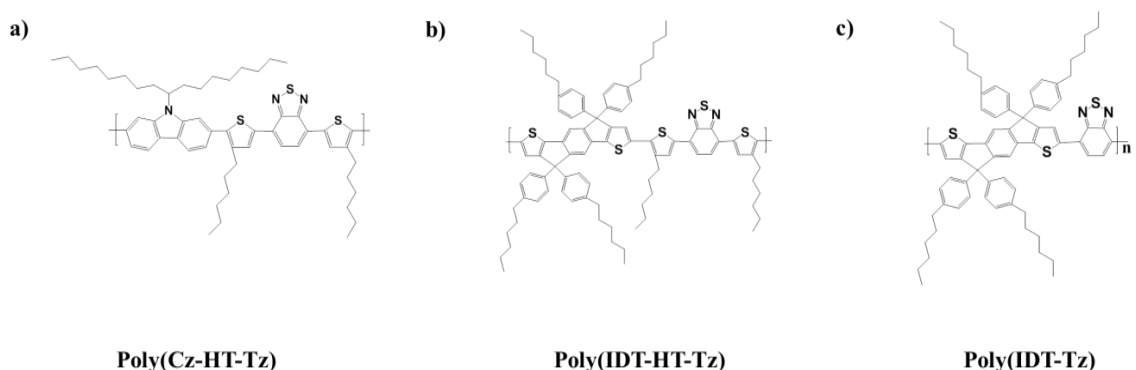


Figure 3.1 Schematic of chemical structures of: a) Poly (Cz-HT-Tz); b) Poly (IDT-HT-Tz) and c) Poly (IDT-Tz)

Chloroform is excellent solvent to those three polymers. However due to its low boiling point (61.2°C), the evaporation process can be rapid and uncontrollable even in FESA system. To this end, toluene (boiling point 110.6°C) has been added to help for better control of patterning morphology. The approximated volume ratio of chloroform/toluene solvent is 1:9 and can be varied for specific polymers. In FESA patterning, each injection

contains 40 μL , 10 mg/mL polymer solution, and the gap height between upper and lower plate is set as 400 μm . The lower plate is programmed to move in “stop – and – move” mode. Different from the continuous move mode that has been applied in the PS system, the lower plate is programmed to stop temporarily by time t between each round of move with distance λ at velocity v . Repeating n round of “stop- and - move” mode, n periodic strips will be formed on the ITO substrate. By adjusting the moving parameters (λ, v, t, n) via computer programming, the height and spacing of the polymer strips can be precisely controlled. Note that although the strips are crafted due to coffee ring effect, fingering instability induced wavelength has also been observed at the edges of the strips. This phenomenon indicates the competition between coffee ring effect and fingering instability occurs during the FESA process, and the dewetting of the polymer solution due to the unfavorable interfacial interaction between the polymer and the substrate^[123].

As an example, the FESA results of Poly (Cz-HT-Tz) are shown in Fig 3.2. Similar to the spin-coated sample in Fig 3.2 a), two distinct colored states and their intermediate color was found the FESA patterned Poly (Cz-HT-Tz) film when the lower half of the glass was dipped into electrolyte to get oxidized while the upper part was remained as natural state (Fig 3.2 b). The intermediate zone between upper and lower half is obtained due to partial oxidization induced by electrolyte vapor. This color change is further confirmed by the absorption peak and intensity change of UV-vis spectroscopy after applying voltage. As the polymer is easily dewetted (see the spin-coated samples in Fig 3.2 a), It's difficult to successfully fabricate Poly (Cz-HT-TZ) strips with small spacing. Characterizations of single strip with AFM (Fig3.2 d) and strip arrays with profilometer (Fig 3.3 e) have shown that the strips are approximately 90 μm in width and 150 nm in height. Besides the profilometer results, the interference experiment also indicates that a good periodicity of the patterns have been successfully maintained. The green diode laser is used as light source and the patterned ITO acts as light grating (Fig 3.2 f). The Intensity of the

interference pattern fades from the center to the two ends due to the coherence of interference and diffraction.

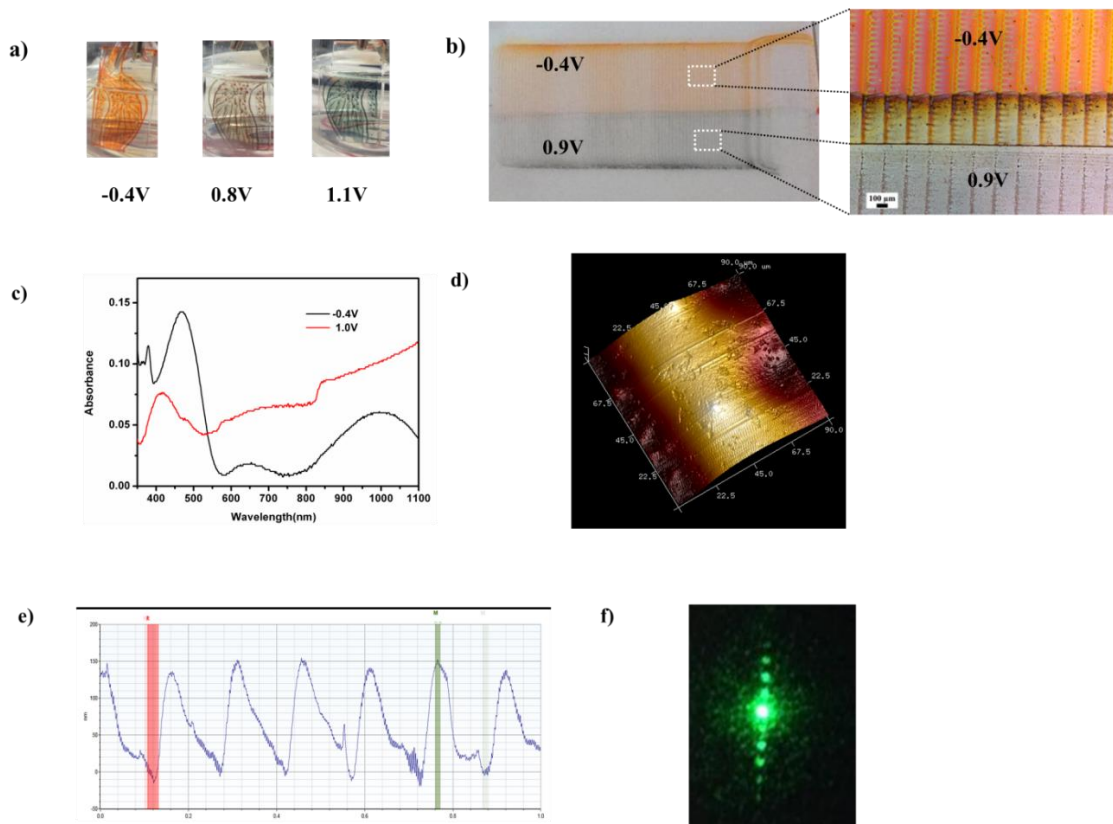


Figure 3.2 a) spin-coated Poly (Cz-HT-Tz) on ITO glasses under neutral, partially oxidized and completely oxidized condition after -0.4V, 0.8V, 1.1V voltage was applied respectively. b) Optical image and micrograph of patterned Poly (Cz-HT-Tz); c) UV-vis NIR spectroelectrochemistry of patterned Poly (Cz-HT-Tz). d) AFM image of patterned Poly (Cz-HT-Tz) strip. e) Profilometer result across an array of Poly (Cz-HT-Tz) strips. f) Interference patterns obtained using a green diode laser illuminating on a neutral patterned Poly (Cz-HT-Tz) film on ITO glass.

To confirm the FESA strategy is generalizable, more ECPs such as Poly (IDT-HT-Tz) and Poly (IDT-Tz) have been successfully patterned on ITO substrate. The patterning results are shown in Fig 3.3 and Fig 3.4, respectively. Note that although intermediate state should exist in the region between the neutral and oxidized part of the sample, the intermediate color in this two situations is not as distinct as Poly (Cz-HT-Tz), thus was not

as significant as in Fig3.2 b). On the other hand, the different color of neutral and oxidized state of Poly (IDT-HT-Tz) and Poly (IDT-Tz) also signify the role that 3-Hexylthiopene (HT) played in adjusting the dual-band of ECPs.

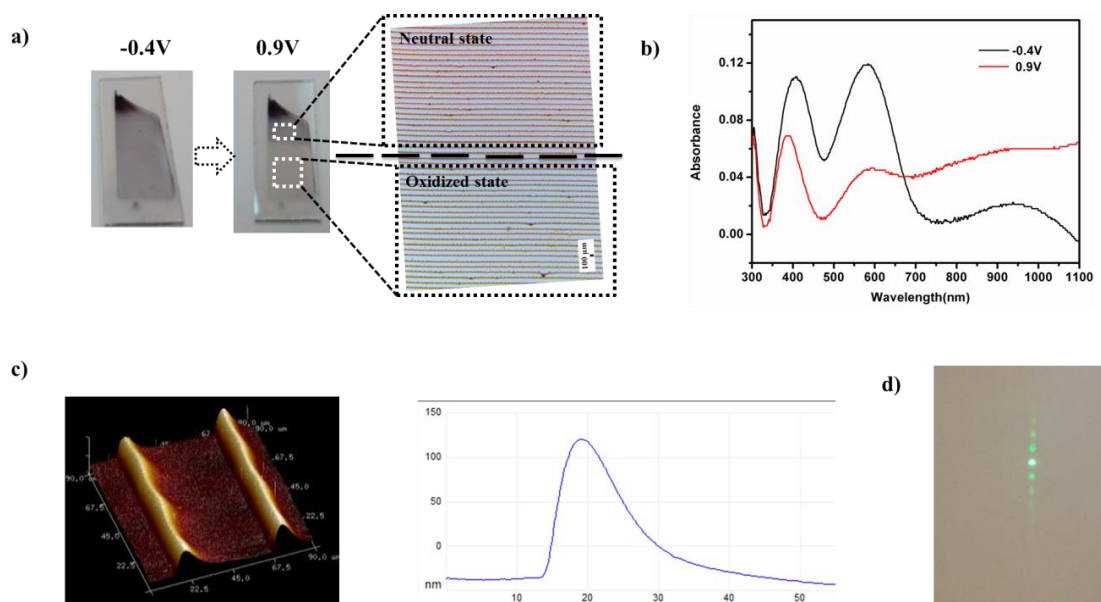


Figure 3.3 a) Optical images and micrographs of patterned Poly (IDT-HT-Tz) under neutral (-0.4V) and completely oxidized state (0.9V) on ITO glasses. b) UV-vis NIR Spectroelectrochemistry of patterned Poly (IDT-HT-Tz). c) AFM image of adjacently patterned Poly (IDT-HT-Tz) strips. d) Interference patterns obtained using a green diode laser illuminating on a neutral patterned Poly (IDT-HT-Tz) film on ITO glass.

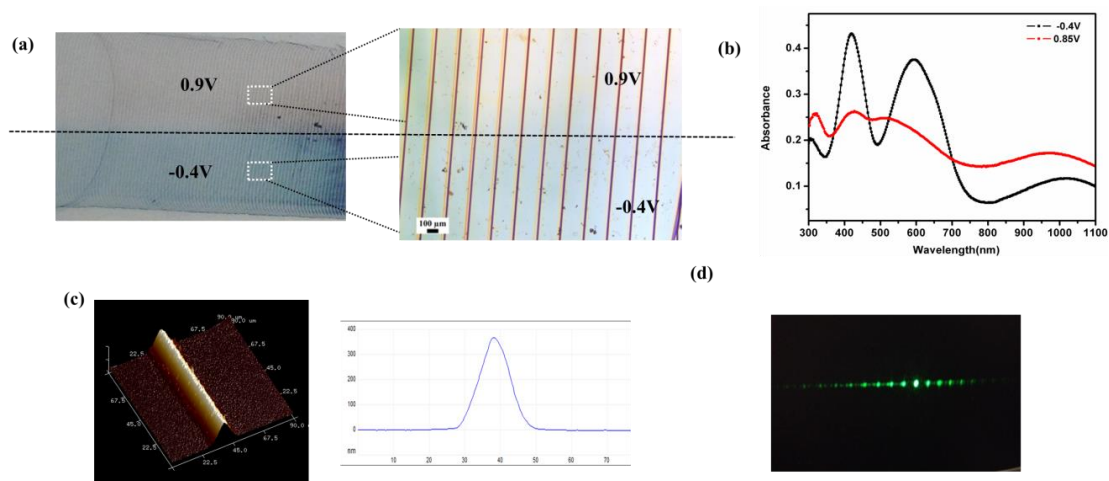


Figure 3.4 a) Optical image and micrograph of patterned Poly (IDT-Tz) under neutral (-0.4V) and completely oxidized state (0.9V) on ITO glasses. b) UV-vis NIR spectroelectrochemistry of patterned Poly (IDT-Tz). c) AFM image of a Poly (IDT-Tz) strip. d) Interference patterns obtained using a green diode laser illuminating on a neutral patterned Poly (IDT-Tz) film on ITO glass.

To further demonstrate that FESA strategies is suitable for any desired substrate, the above three ECPs have been successfully patterned on flexible substrates without losing their electrochromic properties. The substrate is ITO-coated PET thin film. Fig 3.5 shows the patterns before and after external potential applied on flexible substrate. These inspiring results indicate promising potential to apply FESA patterned ECPs in future wearable devices^[113].

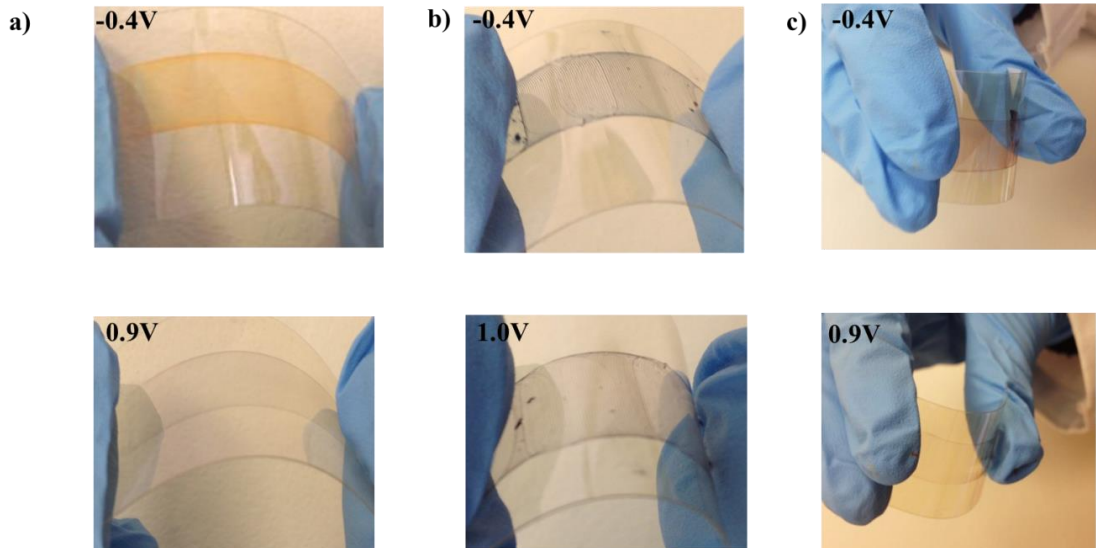


Figure 3.5 Optical images of patterned ECPs films on flexible substrate in neutral state (upper image) and oxidized state (lower image): a) Poly (Cz-HT-Tz); b) Poly (IDT-HT-Tz); c) Poly (IDT-Tz)

In conclusion, flow-enabled self-assembly strategy clearly stands out as a promising alternative to large-scale, periodic strips patterns composed of electrochromic polymers with the retention of their electrochromic performance. The spacing of patterns is well controlled and programmable by adjusting FESA parameters and the whole patterning process is completed in a simple, robust and cost effective manner. Moreover, the capability of patterning ECPs on flexible substrates makes FESA a useful technique for future applications such as wearable devices.

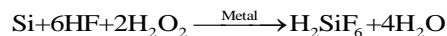
3.3 Silicon Microchannels and Microgratings Templated by Patterns Created via Flow-Enabled Self-Assembly

Surface modification and processing of Silicon (Si) substrate has been attracting numerous research efforts and funding supports due to its direct connection with industry needs. Microchannels with high-aspect-ratio (HAR) on Si substrate, for example, are the basic components of microfluidic technologies such as in-system cooling^[124, 125], biochemical assays^[126, 127], and micro-electromechanical system (MEMS) devices^[128, 129]. Instead of direct surface treatment like E-beam lithography, a mask with desired pattern is always prepared beforehand and fabricated on the surface of Si wafer to protect the covered surface from the following etching steps. On contrary, the bare area will be etched to form channels. To summarize, this Si processing strategy includes 2 key steps, one is mask preparing, and the other one is etching process.

The traditional strategy for HAR microchannels fabrication is photolithography-plasma etching^[130]. In mask preparing step, a PDMS photo-mask with desired patterns is placed over a photosensitive layer (referred as photoresist) coated on Si. When the whole setup is exposed to UV-visible light, the geometry will be transferred to the photoresist layer. However the photoresist layer can be heavily damaged during the following etching process, so that an additional hard etching mask is necessary above the photoresist to protect the desired geometry (See Fig 3.6 a-d). In the etching process, two consecutive plasma etching will be applied in gas chamber, and the uncovered Si surface will be dry-etched to microchannels (See Fig 3.7 left). The aspect ratio of microchannels crafted via photolithography-plasma etching can be as high as 100:1^[131, 132]. However, both mask preparing and etching steps in this method require complicated operation process as well as high instrumental and material costs. Several techniques such as nanoimprint lithograph^[133], KOH etching^[134] and anodic etching^[135] have been developed as alternative to either photolithography or plasma etching, but more expensive treatments are involved and the uniformity of HAR structure is sacrificed.

Recently, newly invented metal-assisted chemical etching (MaCE) has relighted the hope of cost effective etching process^[136, 137]. After desired geometry has been

patterned on the Si surface, a layer of metal catalyst is uniformly deposited on the whole surface of Si wafer. The coated wafer is then placed in hydrofluoric acid (HF) – hydrogen peroxide (H₂O₂) aqueous solution to etch the bared Si surface (Fig 3.7 right). The reaction of the etching process is shown as follows:



To activate the metal catalyst, it has to be directly covered on Si. So the pattern covered Si surface can be blocked from etching. Comparing to dry etching route, in which the surface patterned Si is placed in a gas chamber and gets etched due to plasma attack^[138], MaCE is far more cost effective. Till now, nanowires^[136], nanopores^[139] and 3D nanocavity^[140] with high aspect ratio and submicrometer accuracy have been successfully fabricated by MaCE.

In addition to the advantages associated with of cost effectiveness and easy implementation, high-throughput in one-step of flow-enabled self-assembly (FESA) benefits the mask preparing process, FESA-MaCE turns out to be a novel alternative route for fabricating silicon microchannels. In FESA process, 0.1mg/mL polystyrene- poly (methyl methacrylate) (PS-PMMA) (PS MW= 130K and PMMA MW=133K) toluene solution is chosen to as the block copolymer (BCP) layer for FESA patterning. The (100)-oriented single-crystalline Si wafer is fastened on the lower plate of FESA setup after washed by Piranha solution. The lower plate is programed to be moved in “stop-and-move” mode, while the upper plate remains stationary. During the temporary stop period in each round, the BCP solute gets deposited at the contact line due to coffee ring effect (Fig 3.6 e). Note that almost no fingering instability patterns is observed in the final pattern due to high molecular weight and interfacial properties of PS-PMMA, and thus the uniformity of the strips array can be obtained. The optical micrographs of patterned PS-PMMA on the Si wafer are shown in Fig 3.8. Similarly to *Section 3.2*, the moving parameters of FESA can be easily adjusted to control the final spacing of the periodic strips.

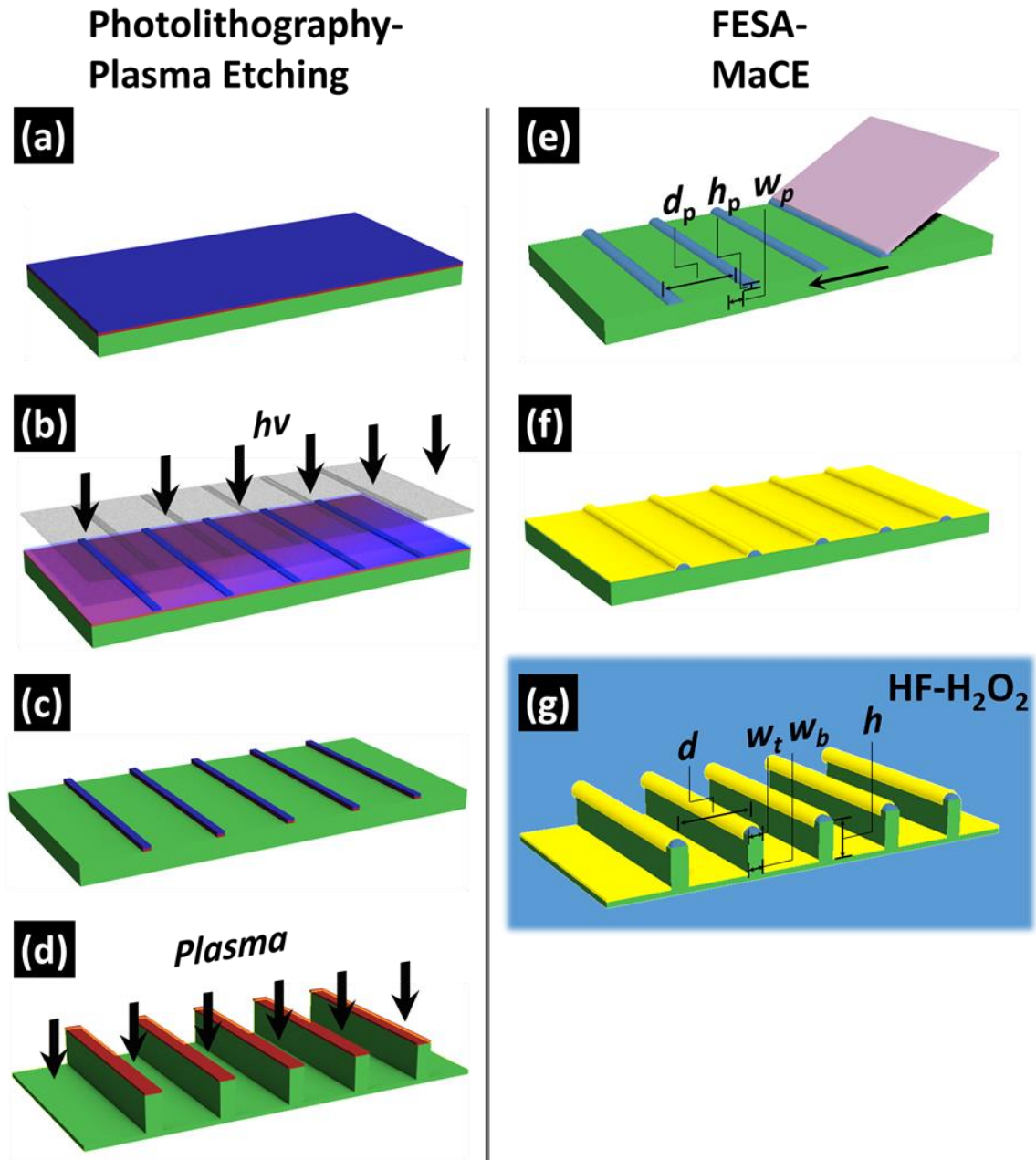


Figure 3.6 Schematic of photolithography-plasma etching route (a-d) and FESA-MaCE route for high aspect ratio microstructures fabrication on Si wafer (e-g)^[141].

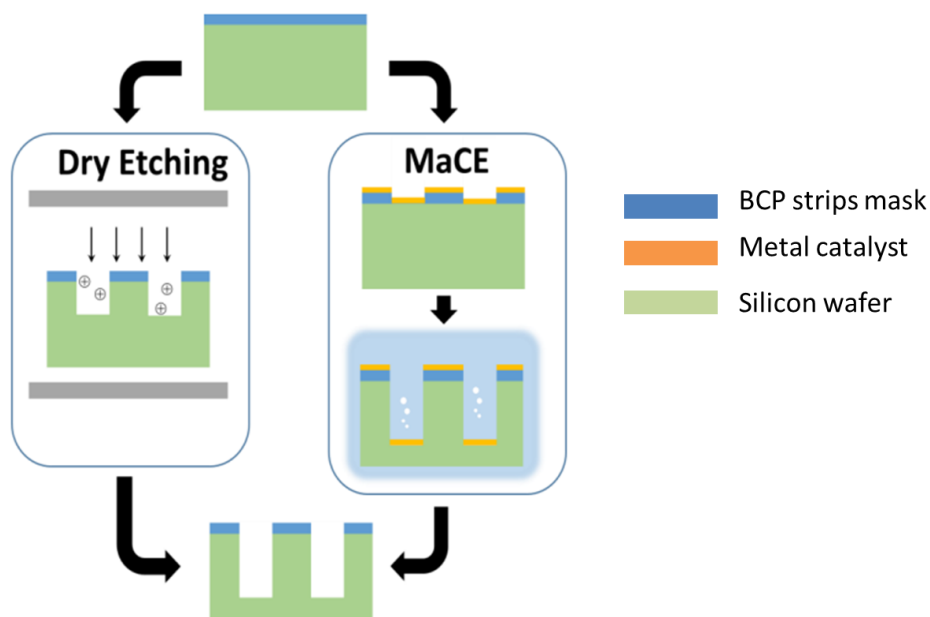


Figure 3.7 Schematic processing flows for day etching (left) and MaCE (right)^[137]



Figure 3.8 Optical micrograph of Si Surface after FESA patterning. The PS-PMMA block copolymer self-assembly appears as periodic lines and the bare Si surface is presented in white color due to light reflection. The scale bar is 100 μm .

To further examine the stability of BCP strips in MaCE solution environment, the Si wafer with the deposited patterned BCP strips is dipped into MaCE solution for 0min, 10min, 20min and 60min. AFM measurement of single BCP strip shows good constancy in width (w_p) and height (h_p) of the strip within the first 10 minutes. Further increase of the immersion time will lead to porous surface structure on the strip starts to show up in AFM profile (Fig 3.9 c and d), indicating damages on the strip. However, the immersion time of real etching process is 10 minutes, thus the stability of the BCP polymer strips is reasonably good in terms of MaCE solution resistance.

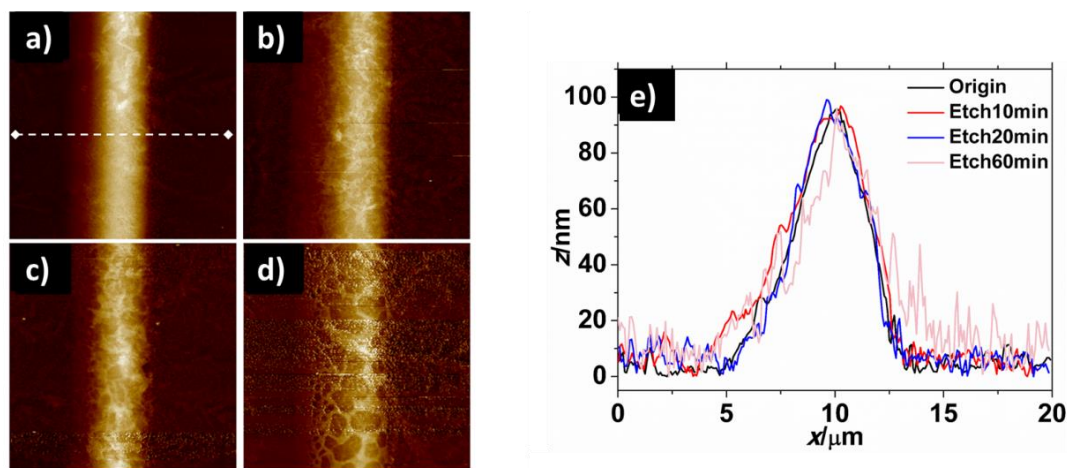


Figure 3.9 AFM images of polymer strip after immersion in MaCE for a) 0min; b) 10min; c) 20min; d) 60min. The corresponding AFM cross sections are shown in e).^[141]

Before coating the metal catalyst, Ar/O₂ plasma is used to clean the trace amount of residue polymer between strips (i.e. the descum process). The width (w_p) and height (h_p) of the strips turn out to decrease with the increase of plasma exposing time (Fig 3.10). Similar results have been reported in plasma treated PS microsphere^[142]. On the other hand, the experimental results serve as a good example that the mask materials in dry etching route will be continuously damaged during the plasma treatment. Besides, The nature of flow enabled self-assembly makes it difficult to craft strips with width less than

its critical value (see *Section 2.2*)^[38]. To overcome this limitation, the descum process can also help obtain thinner strips and thus wider channels after etching.

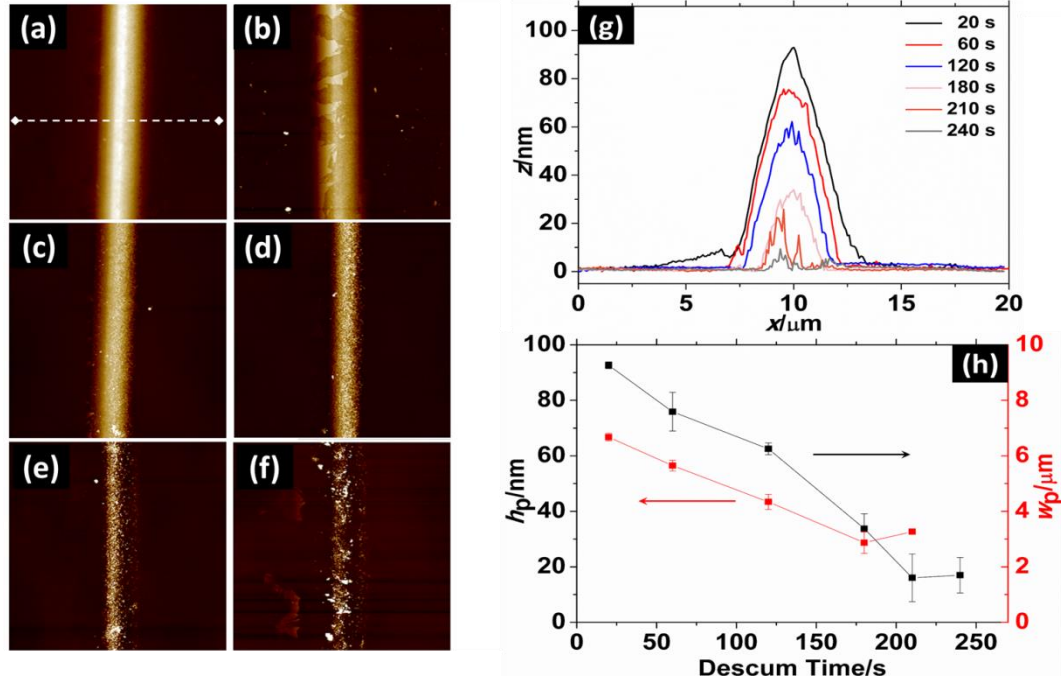


Figure 3.10 a-f) AFM images of patterned BCP strips after descum process of : a) 20 s; b) 60 s; c) 120 s; d) 180 s; e) 210 s and f) 240 s. The corresponding cross section profiles is shown in g), and the relationship between descum time and width (w_p) and height (h_p) of the strip is shown in h)^[141].

After FESA and descum process, nano-porous Au thin film with thickness about 14.3 nm is coated on the sample and then the Si wafer is etched in MaCE solution for 10 minutes. The cross sectional SEM images of samples with different descum time are shown in Fig 3.11. It's clear that increasing descum time can help reduce the width of the micrograding. The FESA crafted BCP strips can be observed on the top of each grades, and successfully protect the covered Si surface from further etching. Interestingly, the cross section of the micrograding is trapezoid, i.e., the w_t is always less than w_b . This is due to the different real time etching rate on the sidewall of the microgradings.

In conclusion, FESA-MaCE is a facile and low-cost route to fabricating large-scale periodic microchannels. The aspect ratio of final microgradings is up to 16:1 and lateral edge roughness is below $0.5\mu m$.^[141] In particular, the PS-PMMA strips crafted via flow-enabled self-assembly serve as the etching mask, and have shown reasonable resistance in MaCE solution environment. FESA parameters and descum time can directly control the spacing of the BCP strips and thus the final etched microchannels. The integration of FESA and MaCE will open a new avenue to create various polymer-based self-assembled patterns for use in Si etching.

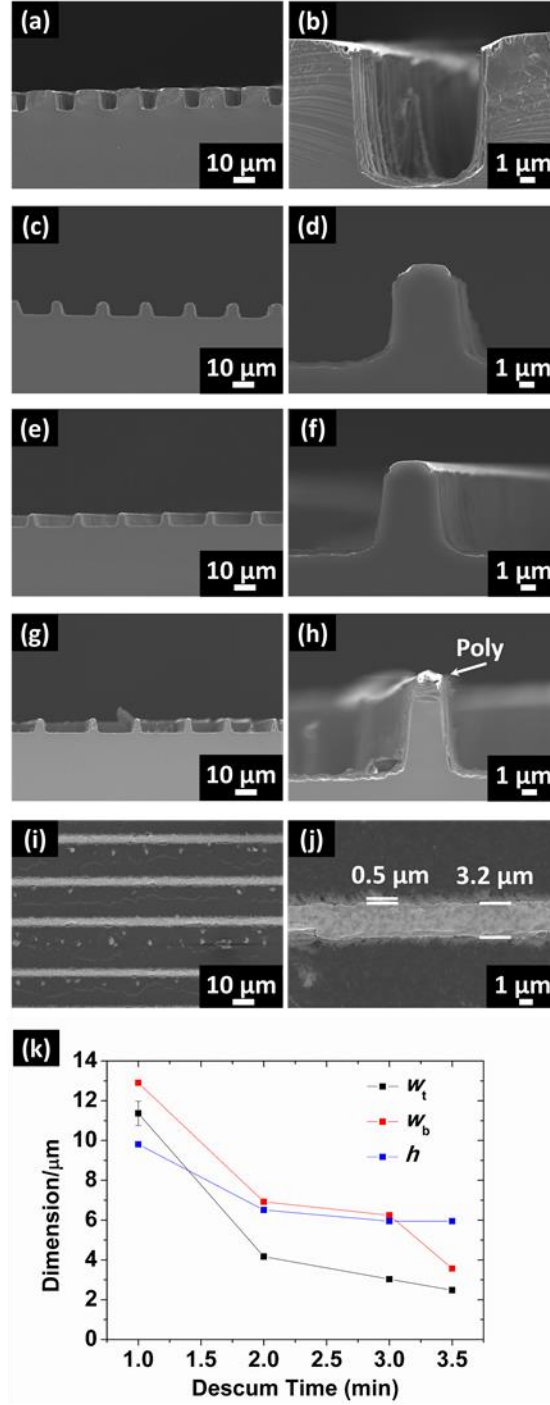


Figure 3.11 Cross sectional SEM images of Si sample after FESA and MaCE for 10 with descum time of a) 1 min, c) 2 min, e) 3 min and g) 3.5 min. and their corresponding high magnifications in b), d), f) and h). Top-view SEM image of sample in e) is shown in i) and j). The w_t , w_b and h of each sample are plotted versus their corresponding descum time. “Poly” in h) refers to the polymer strips crafted via FESA.^[141]

CHAPTER 4

CONCLUSIONS

4.1 Thesis Review

In this thesis, the mechanism of pattern transition from spoke to strip in polystyrene system and the applications of patterns crafted by flow-enabled self-assembly have been discussed.

In the mechanism section, theoretical and experimental studies showed that the final structures (i.e., coffee ring induced spoke pattern, fingering instability induced strip pattern, and their intermediate network-like structures) can be coherently determined by the molecular weight of polystyrene, the initial concentration of solution c and the velocity of the lower plate v . Furthermore, changing these three parameters can lead to the changes in capillarity number, and that the solution with lower capillarity number was more prone to form spokes, that is, fingering instability-dominated pattern. A hypothesis of minimum finger width below which spoke patterns will not be formed is proposed base on experimental results and previous theoretical studies. While the λ_{c-c} of spokes decreased with increase in the moving speed of lower plate due to less deposition at the low speed, the λ_{c-c} of strips will first decrease and then increase with the increase of the moving speed of lower plate as a result of the its sessile moving mode at low v and pendant moving mode at high v . The relationship between the strip width and the moving velocity shows consistency with previous research on PMMA system. This research shed some light on the mechanism of different patterns crafted by FESA and provides useful guidance for predicting the final patterns obtained experimentally.

In the application section, direct and indirect uses of the patterned polymer strips via FESA method have been demonstrated. As an example of direct use, three

electrochromic polymers have been successfully patterned on ITO glass and flexible substrate without losing their electrochromism properties. In the case of Si etching, FESA patterned PS-PMMA strips act as mask to protect the desired geometry on Si wafer, and a large scale processed Si wafer with uniform microchannels on it has been successfully fabricated by integrating FESA and MaCE techniques. In both applications, the lower plate of FESA is programmed to move in “stop-and-move” mode and the spacing of the polymer strips is precisely controlled by FESA parameters such as moving velocity v , stop time t , single-round move distance λ and round number n . Both applications convincingly demonstrate the advantages of cost effective, large yield and flexible control of flow-enabled self-assembly.

4.2 Future Work

More experiments are needed to prove the hypothesis of minimum finger width in polystyrene system. More parameters such as local vapor concentration of toluene, humidity, temperature and the gap distance between the upper and lower plates may be related to the pattern transition and should be studied in depth. The mechanism of the evaporation behavior during FESA process can be further studied by expending the same methodology of PS toluene solution to other polymer solutions. FESA is also amenable to craft intriguing structures of other functional polymers. Hierarchical structures maybe induced by patterning solutions or suspensions containing multiple solutes or multiple solvents on substrates with different surface treatments. Besides, the nature that FESA has almost no restriction to the properties of the substrate opens up more opportunities for other research such as wrinkle structure (induced when release the two ends of elongated PDMS substrate after FESA patterning).

REFERENCES

- [1] Whitesides, G. M.; Grzybowski, B., Self-assembly at all scales. *Science* **2002**, 295 (5564), 2418-2421.
- [2] Park, C.; Yoon, J.; Thomas, E. L., Enabling nanotechnology with self assembled block copolymer patterns. *Polymer* **2003**, 44 (22), 6725-6760.
- [3] Byun, M.; Bowden, N. B.; Lin, Z., Hierarchically organized structures engineered from controlled evaporative self-assembly. *Nano letters* **2010**, 10 (8), 3111-3117.
- [4] Wild, B.; Cao, L.; Sun, Y.; Khanal, B. P.; Zubarev, E. R.; Gray, S. K.; Scherer, N. F.; Pelton, M., Propagation lengths and group velocities of plasmons in chemically synthesized gold and silver nanowires. *ACS nano* **2012**, 6 (1), 472-482.
- [5] Zubarev, E. R.; Talroze, R. V.; Yuranova, T. I.; Plate, N. A.; Finkelmann, H., Influence of network topology on polydomain-monodomain transition in side chain liquid crystalline elastomers with cyanobiphenyl mesogens. *Macromolecules* **1998**, 31 (11), 3566-3570.
- [6] Whitesides, G. M.; Kriebel, J. K.; Mayers, B. T., Self-assembly and nanostructured materials. In *Nanoscale Assembly*, Springer: 2005; pp 217-239.
- [7] Park, J. W.; Thomas, E. L., Multiple ordering transitions: Hierarchical self - assembly of rod - coil block copolymers. *Advanced Materials* **2003**, 15 (7 - 8), 585-588.
- [8] Wong, G. C.; Tang, J. X.; Lin, A.; Li, Y.; Janmey, P. A.; Safinya, C. R., Hierarchical self-assembly of F-actin and cationic lipid complexes: stacked three-layer tubule networks. *Science* **2000**, 288 (5473), 2035-2039.

- [9] Cölfen, H.; Mann, S., Higher - order organization by mesoscale self - assembly and transformation of hybrid nanostructures. *Angewandte Chemie International Edition* **2003**, 42 (21), 2350-2365.
- [10] Xia, Y.; Whitesides, G. M., Soft lithography. *Annual review of materials science* **1998**, 28 (1), 153-184.
- [11] Park, S.; Kim, B.; Yavuzcetin, O.; Tuominen, M. T.; Russell, T. P., Ordering of PS-b-P4VP on patterned silicon surfaces. *ACS nano* **2008**, 2 (7), 1363-1370.
- [12] Chen, X.; Lenhert, S.; Hirtz, M.; Lu, N.; Fuchs, H.; Chi, L., Langmuir–Blodgett patterning: a bottom–up way to build mesostructures over large areas. *Accounts of chemical research* **2007**, 40 (6), 393-401.
- [13] Köpf, M. H.; Harder, H.; Reiche, J. r.; Santer, S., Impact of Temperature on the LB Patterning of DPPC on Mica. *Langmuir* **2011**, 27 (20), 12354-12360.
- [14] Li, L.; Köpf, M. H.; Gurevich, S. V.; Friedrich, R.; Chi, L., Structure Formation by Dynamic Self - Assembly. *Small* **2012**, 8 (4), 488-503.
- [15] Shereda, L. T.; Larson, R. G.; Solomon, M. J., Local stress control of spatiotemporal ordering of colloidal crystals in complex flows. *Physical review letters* **2008**, 101 (3), 038301.
- [16] Böker, A.; He, J.; Emrick, T.; Russell, T. P., Self-assembly of nanoparticles at interfaces. *Soft Matter* **2007**, 3 (10), 1231-1248.
- [17] Binks, B. P., Particles as surfactants—similarities and differences. *Current opinion in colloid & interface science* **2002**, 7 (1), 21-41.
- [18] Lumsdon, S. O.; Kaler, E. W.; Velev, O. D., Two-dimensional crystallization of microspheres by a coplanar AC electric field. *Langmuir* **2004**, 20 (6), 2108-2116.

- [19] Ding, T.; Song, K.; Clays, K.; Tung, C. H., Fabrication of 3D Photonic Crystals of Ellipsoids: Convective Self - Assembly in Magnetic Field. *Advanced Materials* **2009**, *21* (19), 1936-1940.
- [20] Mittal, M.; Furst, E. M., Electric Field - Directed Convective Assembly of Ellipsoidal Colloidal Particles to Create Optically and Mechanically Anisotropic Thin Films. *Advanced Functional Materials* **2009**, *19* (20), 3271-3278.
- [21] Han, W.; Lin, Z., Learning from “Coffee Rings” : Ordered Structures Enabled by Controlled Evaporative Self - Assembly. *Angewandte Chemie International Edition* **2012**, *51* (7), 1534-1546.
- [22] Lin, Z., *Evaporative self-assembly of ordered complex structures*. World Scientific: 2012.
- [23] Brinker, C. J.; Lu, Y.; Sellinger, A.; Fan, H., Evaporation-induced self-assembly: nanostructures made easy. *Advanced materials* **1999**, *11* (7), 579-585.
- [24] Deegan, R. D.; Bakajin, O.; Dupont, T. F.; Huber, G.; Nagel, S. R.; Witten, T. A., Capillary flow as the cause of ring stains from dried liquid drops. *Nature* **1997**, *389* (6653), 827-829.
- [25] Wong, T.-S.; Chen, T.-H.; Shen, X.; Ho, C.-M., Nanochromatography driven by the coffee ring effect. *Analytical chemistry* **2011**, *83* (6), 1871-1873.
- [26] Choi, S.; Stassi, S.; Pisano, A. P.; Zohdi, T. I., Coffee-ring effect-based three dimensional patterning of micro/nanoparticle assembly with a single droplet. *Langmuir* **2010**, *26* (14), 11690-11698.
- [27] Sempels, W.; De Dier, R.; Mizuno, H.; Hofkens, J.; Vermant, J., Auto-production of biosurfactants reverses the coffee ring effect in a bacterial system. *Nature communications* **2013**, *4*, 1757.

- [28] Deegan, R. D., Pattern formation in drying drops. *Physical review E* **2000**, *61* (1), 475.
- [29] Lin, Y.; Böker, A.; He, J.; Sill, K.; Xiang, H.; Abetz, C.; Li, X.; Wang, J.; Emrick, T.; Long, S., Self-directed self-assembly of nanoparticle/copolymer mixtures. *Nature* **2005**, *434* (7029), 55-59.
- [30] Kim, Y.; Han, H.; Kim, Y.; Lee, W.; Alexe, M.; Baik, S.; Kim, J. K., Ultrahigh density array of epitaxial ferroelectric nanoislands on conducting substrates. *Nano letters* **2010**, *10* (6), 2141-2146.
- [31] Park, S.; Lim, J.-H.; Chung, S.-W.; Mirkin, C. A., Self-assembly of mesoscopic metal-polymer amphiphiles. *Science* **2004**, *303* (5656), 348-351.
- [32] Yabu, H.; Shimomura, M., Preparation of Self - Organized Mesoscale Polymer Patterns on a Solid Substrate: Continuous Pattern Formation from a Receding Meniscus. *Advanced Functional Materials* **2005**, *15* (4), 575-581.
- [33] Kim, H. S.; Lee, C. H.; Sudeep, P.; Emrick, T.; Crosby, A. J., Nanoparticle stripes, grids, and ribbons produced by flow coating. *Advanced Materials* **2010**, *22* (41), 4600-4604.
- [34] Xu, J.; Xia, J.; Hong, S. W.; Lin, Z.; Qiu, F.; Yang, Y., Self-assembly of gradient concentric rings via solvent evaporation from a capillary bridge. *Physical review letters* **2006**, *96* (6), 066104.
- [35] Xu, J.; Xia, J.; Lin, Z., Evaporation - Induced Self - Assembly of Nanoparticles from a Sphere - on - Flat Geometry. *Angewandte Chemie* **2007**, *119* (11), 1892-1895.
- [36] Hong, S. W.; Xia, J.; Lin, Z., Spontaneous formation of mesoscale polymer patterns in an evaporating bound solution. *Advanced Materials* **2007**, *19* (10), 1413-1417.

- [37] Hong, S. W.; Jeong, W.; Ko, H.; Kessler, M. R.; Tsukruk, V. V.; Lin, Z., Directed self-assembly of gradient concentric carbon nanotube rings. **2008**.
- [38] Li, B. Crafting Ordered Structures of Nanomaterials via Flow-Enabled Self-Assembly (FESA) and Controlled Evaporative Self-Assembly (CESA). Dissertation, Georgia Institute of Technology, Georgia Institute of Technology, 2015.
- [39] Langmuir, I., The evaporation of small spheres. *Physical review* **1918**, 12 (5), 368.
- [40] Poulard, C.; Cazabat, A., Diffusion-driven evaporation of sessile drops. *Journal of Physics: Condensed Matter* **2005**, 17 (49), S4213.
- [41] Knacke, O.; Stranski, I., The mechanism of evaporation. *Progress in Metal Physics* **1956**, 6, 181-235.
- [42] Cazabat, A.-M.; Guéna, G., Evaporation of macroscopic sessile droplets. *Soft Matter* **2010**, 6 (12), 2591-2612.
- [43] Frohn, A.; Roth, N., *Dynamics of droplets*. Springer Science & Business Media: 2000.
- [44] Semenov, S.; Starov, V.; Rubio, R.; Velarde, M., Instantaneous distribution of fluxes in the course of evaporation of sessile liquid droplets: computer simulations. *Colloids and Surfaces A: Physicochemical and Engineering Aspects* **2010**, 372 (1), 127-134.
- [45] Hu, H.; Larson, R. G., Evaporation of a sessile droplet on a substrate. *The Journal of Physical Chemistry B* **2002**, 106 (6), 1334-1344.
- [46] Murisic, N.; Kondic, L., On evaporation of sessile drops with moving contact lines. *Journal of Fluid Mechanics* **2011**, 679, 219-246.

- [47] Siregar, D.; Kuerten, J.; van der Geld, C., Numerical simulation of the drying of inkjet-printed droplets. *Journal of colloid and interface science* **2013**, 392, 388-395.
- [48] Haut, B.; Colinet, P., Surface-tension-driven instabilities of a pure liquid layer evaporating into an inert gas. *Journal of colloid and interface science* **2005**, 285 (1), 296-305.
- [49] Burelbach, J. P.; Bankoff, S. G.; Davis, S. H., Nonlinear stability of evaporating/condensing liquid films. *Journal of Fluid Mechanics* **1988**, 195, 463-494.
- [50] Oron, A.; Davis, S. H.; Bankoff, S. G., Long-scale evolution of thin liquid films. *Reviews of modern physics* **1997**, 69 (3), 931.
- [51] Dehaeck, S.; Rednikov, A.; Colinet, P., Vapor-based interferometric measurement of local evaporation rate and interfacial temperature of evaporating droplets. *Langmuir* **2014**, 30 (8), 2002-2008.
- [52] Dehaeck, S.; Colinet, P. In *Measuring Vapour Cloud Concentrations with Digital Holography*, Digital Holography and Three-Dimensional Imaging, Optical Society of America: 2012; p DTu2C. 2.
- [53] Fischer, B. J., Particle convection in an evaporating colloidal droplet. *Langmuir* **2002**, 18 (1), 60-67.
- [54] Bodiguel, H.; Leng, J., Imaging the drying of a colloidal suspension: Velocity field. *Chemical Engineering and Processing: Process Intensification* **2013**, 68, 60-63.
- [55] Chaudhury, M. K.; Whitesides, G. M., How to make water run uphill. *Science* **1992**, 256 (5063), 1539-1541.

- [56] Hu, H.; Larson, R. G., Analysis of the effects of Marangoni stresses on the microflow in an evaporating sessile droplet. *Langmuir* **2005**, *21* (9), 3972-3980.
- [57] Gugliotti, M.; Silverstein, T., Tears of wine. *Journal of chemical education* **2004**, *81* (1), 67.
- [58] Scriven, L.; Sternling, C., The marangoni effects. **1960**.
- [59] Buffone, C.; Sefiane, K., Investigation of thermocapillary convective patterns and their role in the enhancement of evaporation from pores. *International Journal of Multiphase Flow* **2004**, *30* (9), 1071-1091.
- [60] Buffone, C.; Sefiane, K.; Christy, J., Experimental investigation of self-induced thermocapillary convection for an evaporating meniscus in capillary tubes using micro-particle image velocimetry. *Physics of Fluids (1994-present)* **2005**, *17* (5), 052104.
- [61] Buffone, C.; Sefiane, K., IR measurements of interfacial temperature during phase change in a confined environment. *Experimental thermal and fluid science* **2004**, *29* (1), 65-74.
- [62] Pearson, J., On convection cells induced by surface tension. *Journal of fluid mechanics* **1958**, *4* (05), 489-500.
- [63] Nield, D., Surface tension and buoyancy effects in cellular convection. *Journal of Fluid Mechanics* **1964**, *19* (03), 341-352.
- [64] Thompson, I.; Duan, F.; Ward, C., Absence of Marangoni convection at Marangoni numbers above 27,000 during water evaporation. *Physical Review E* **2009**, *80* (5), 056308.
- [65] Steinchen, A.; Sefiane, K., Self-organised Marangoni motion at evaporating drops or in capillary menisci-thermohydrodynamical model. *Journal of Non-Equilibrium Thermodynamics* **2005**, *30* (1), 39-51.

- [66] Hu, Y.-C.; Zhou, Q.; Ye, H.-M.; Wang, Y.-F.; Cui, L.-S., Peculiar surface profile of poly (ethylene oxide) film with ring-like nucleation distribution induced by Marangoni flow effect. *Colloids and Surfaces A: Physicochemical and Engineering Aspects* **2013**, 428, 39-46.
- [67] Barash, L. Y.; Bigioni, T.; Vinokur, V.; Shchur, L., Evaporation and fluid dynamics of a sessile drop of capillary size. *Physical Review E* **2009**, 79 (4), 046301.
- [68] Xu, X.; Luo, J.; Guo, D., Criterion for reversal of thermal Marangoni flow in drying drops. *Langmuir* **2009**, 26 (3), 1918-1922.
- [69] Hu, H.; Larson, R. G., Marangoni effect reverses coffee-ring depositions. *The Journal of Physical Chemistry B* **2006**, 110 (14), 7090-7094.
- [70] Bhardwaj, R.; Fang, X.; Somasundaran, P.; Attinger, D., Self-assembly of colloidal particles from evaporating droplets: role of DLVO interactions and proposition of a phase diagram. *Langmuir* **2010**, 26 (11), 7833-7842.
- [71] Yunker, P. J.; Still, T.; Lohr, M. A.; Yodh, A., Suppression of the coffee-ring effect by shape-dependent capillary interactions. *Nature* **2011**, 476 (7360), 308-311.
- [72] Loudet, J.-C.; Yodh, A. G.; Poulligny, B., Wetting and contact lines of micrometer-sized ellipsoids. *Physical review letters* **2006**, 97 (1), 018304.
- [73] Anyfantakis, M.; Baigl, D., Dynamic Photocontrol of the Coffee - Ring Effect with Optically Tunable Particle Stickiness. *Angewandte Chemie* **2014**, 126 (51), 14301-14305.
- [74] Popov, Y. O., Evaporative deposition patterns: spatial dimensions of the deposit. *Physical Review E* **2005**, 71 (3), 036313.

- [75] Li, B.; Han, W.; Jiang, B.; Lin, Z., Crafting threads of diblock copolymer micelles via flow-enabled self-assembly. *ACS nano* **2014**, 8 (3), 2936-2942.
- [76] Carvalho, M. S.; Kheshgi, H. S., Low - flow limit in slot coating: Theory and experiments. *AIChE journal* **2000**, 46 (10), 1907-1917.
- [77] Lee, K.-Y.; Liu, L.-D.; Ta-Jo, L., Minimum wet thickness in extrusion slot coating. *Chemical Engineering Science* **1992**, 47 (7), 1703-1713.
- [78] Stafford, C. M.; Roskov, K. E.; Epps III, T. H.; Fasolka, M. J., Generating thickness gradients of thin polymer films via flow coating. *Review of scientific instruments* **2006**, 77 (2), 023908.
- [79] Durst, F.; Wagner, H.-G., Slot coating. In *Liquid Film Coating*, Springer: 1997; pp 401-426.
- [80] Yabu, H.; Inoue, K.; Shimomura, M., Multiple-periodic structures of self-organized honeycomb-patterned films and polymer nanoparticles hybrids. *Colloids and Surfaces A: Physicochemical and Engineering Aspects* **2006**, 284, 301-304.
- [81] Tsuruma, A.; Tanaka, M.; Yamamoto, S.; Fukushima, N.; Yabu, H.; Shimomura, M., Topographical control of neurite extension on stripe-patterned polymer films. *Colloids and Surfaces A: Physicochemical and Engineering Aspects* **2006**, 284, 470-474.
- [82] Li, B.; Zhang, C.; Jiang, B.; Han, W.; Lin, Z., Flow - Enabled Self - Assembly of Large - Scale Aligned Nanowires. *Angewandte Chemie International Edition* **2015**, 54 (14), 4250-4254.
- [83] Li, B.; Han, W.; Byun, M.; Zhu, L.; Zou, Q.; Lin, Z., Macroscopic highly aligned DNA nanowires created by controlled evaporative self-assembly. *ACS nano* **2013**, 7 (5), 4326-4333.

[84] Han, W. Learning from "Coffee Rings": Ordered Structures Enabled by Controlled Evaporative Self-Assembly. Doctor of Philosophy, Iowa State University, 2012.

[85] Hong, S. W.; Xia, J.; Byun, M.; Zou, Q.; Lin, Z., Mesoscale patterns formed by evaporation of a polymer solution in the proximity of a sphere on a smooth substrate: molecular weight and curvature effects. *Macromolecules* **2007**, *40* (8), 2831-2836.

[86] Poh, B.; Ong, B., Dependence of viscosity of polystyrene solutions on molecular weight and concentration. *European polymer journal* **1984**, *20* (10), 975-978.

[87] Lyushnin, A.; Golovin, A.; Pismen, L., Fingering instability of thin evaporating liquid films. *Physical Review E* **2002**, *65* (2), 021602.

[88] Hong, S. W.; Giri, S.; Lin, V. S.-Y.; Lin, Z., Simple route to gradient concentric metal and metal oxide rings. *Chemistry of materials* **2006**, *18* (22), 5164-5166.

[89] Chen, X.; Lu, N.; Zhang, H.; Hirtz, M.; Wu, L.; Fuchs, H.; Chi, L., Langmuir-Blodgett patterning of phospholipid microstripes: Effect of the second component. *The Journal of Physical Chemistry B* **2006**, *110* (15), 8039-8046.

[90] Cazabat, A.; Heslot, F.; Carles, P.; Troian, S., Hydrodynamic fingering instability of driven wetting films. *Advances in colloid and interface science* **1992**, *39*, 61-75.

[91] Kataoka, D. E.; Troian, S. M., A theoretical study of instabilities at the advancing front of thermally driven coating films. *Journal of colloid and interface science* **1997**, *192* (2), 350-362.

[92] Kataoka, D. E.; Troian, S. M., Stabilizing the advancing front of thermally driven climbing films. *Journal of colloid and interface science* **1998**, *203* (2), 335-344.

- [93] Bertozzi, A. L.; Brenner, M. P., Linear stability and transient growth in driven contact lines. *Physics of Fluids (1994-present)* **1997**, 9 (3), 530-539.
- [94] Huppert, H. E., Flow and instability of a viscous current down a slope. *Nature* **1982**, 300 (5891), 427-429.
- [95] Cheng, X.; Xu, L.; Patterson, A.; Jaeger, H. M.; Nagel, S. R., Towards the zero-surface-tension limit in granular fingering instability. *Nature Physics* **2008**, 4 (3), 234-237.
- [96] Kataoka, D. E.; Troian, S. M., Patterning liquid flow on the microscopic scale. *Nature* **1999**, 402 (6763), 794-797.
- [97] Zik, O.; Olami, Z.; Moses, E., Fingering instability in combustion. *Physical review letters* **1998**, 81 (18), 3868.
- [98] Kulicke, W.-M.; Kniewske, R., The shear viscosity dependence on concentration, molecular weight, and shear rate of polystyrene solutions. *Rheologica acta* **1984**, 23 (1), 75-83.
- [99] Milas, M.; Rinaudo, M.; Tinland, B., The viscosity dependence on concentration, molecular weight and shear rate of xanthan solutions. *Polymer Bulletin* **1985**, 14 (2), 157-164.
- [100] Alfrey, T.; Bartovics, A.; Mark, H., The Effect of Temperature and Solvent Type on the Intrinsic Viscosity of High-Polymer Solutions. *Rubber Chemistry and Technology* **1942**, 15 (4), 820-825.
- [101] Li, B., Crafting Ordered Structures of Nanomaterial via Flow-Enabled Self-Assembly (FESA) and Controlled Evaporative Self-Assembly (CESA). Georgia Institute of Technology: 2015.

- [102] Tseng, A.; Chen, K.; Chen, C. D.; Ma, K. J., Electron beam lithography in nanoscale fabrication: recent development. *Electronics Packaging Manufacturing, IEEE Transactions on* **2003**, 26 (2), 141-149.
- [103] Piner, R. D.; Zhu, J.; Xu, F.; Hong, S.; Mirkin, C. A., " Dip-pen" nanolithography. *Science* **1999**, 283 (5402), 661-663.
- [104] Levenson, M. D.; Viswanathan, N.; Simpson, R., Improving resolution in photolithography with a phase-shifting mask. *Electron Devices, IEEE Transactions on* **1982**, 29 (12), 1828-1836.
- [105] Jacobs, H. O.; Whitesides, G. M., Submicrometer patterning of charge in thin-film electrets. *Science* **2001**, 291 (5509), 1763-1766.
- [106] Erdogan, B.; Song, L.; Wilson, J. N.; Park, J. O.; Srinivasarao, M.; Bunz, U. H., Permanent Bubble Arrays from a Cross-Linked Poly (p ara-phenyleneethynylene): Picoliter Holes without Microfabrication. *Journal of the American Chemical Society* **2004**, 126 (12), 3678-3679.
- [107] McDonald, J. C.; Whitesides, G. M., Poly (dimethylsiloxane) as a material for fabricating microfluidic devices. *Accounts of chemical research* **2002**, 35 (7), 491-499.
- [108] Granqvist, C. G., *Handbook of inorganic electrochromic materials*. Elsevier: 1995.
- [109] Jensen, J.; Krebs, F. C., From the bottom up—flexible solid state electrochromic devices. *Advanced Materials* **2014**, 26 (42), 7231-7234.
- [110] Yang, X.; Zhu, G.; Wang, S.; Zhang, R.; Lin, L.; Wu, W.; Wang, Z. L., A self-powered electrochromic device driven by a nanogenerator. *Energy & Environmental Science* **2012**, 5 (11), 9462-9466.
- [111] Dyer, A. L.; Bulloch, R. H.; Zhou, Y.; Kippelen, B.; Reynolds, J. R.; Zhang, F., A Vertically Integrated Solar - Powered Electrochromic Window

for Energy Efficient Buildings. *Advanced Materials* **2014**, 26 (28), 4895-4900.

[112] Beaujuge, P. M.; Reynolds, J. R., Color control in π -conjugated organic polymers for use in electrochromic devices. *Chemical reviews* **2010**, 110 (1), 268-320.

[113] Somani, P. R.; Radhakrishnan, S., Electrochromic materials and devices: present and future. *Materials chemistry and physics* **2003**, 77 (1), 117-133.

[114] Kerszulis, J. A.; Amb, C. M.; Dyer, A. L.; Reynolds, J. R., Follow the Yellow Brick Road: Structural Optimization of Vibrant Yellow-to-Transmissive Electrochromic Conjugated Polymers. *Macromolecules* **2014**, 47 (16), 5462-5469.

[115] Beverina, L.; Pagani, G.; Sassi, M., Multichromophoric electrochromic polymers: colour tuning of conjugated polymers through the side chain functionalization approach. *Chemical Communications* **2014**, 50 (41), 5413-5430.

[116] Beaujuge, P. M.; Vasilyeva, S. V.; Ellinger, S.; McCarley, T. D.; Reynolds, J. R., Unsaturated Linkages in Dioxothiophene– Benzothiadiazole Donor– Acceptor Electrochromic Polymers: The Key Role of Conformational Freedom. *Macromolecules* **2009**, 42 (11), 3694-3706.

[117] Amb, C. M.; Beaujuge, P. M.; Reynolds, J. R., Spray - Processable Blue - to - Highly Transmissive Switching Polymer Electrochromes via the Donor – Acceptor Approach. *Advanced Materials* **2010**, 22 (6), 724-728.

[118] Shi, P.; Amb, C. M.; Knott, E. P.; Thompson, E. J.; Liu, D. Y.; Mei, J.; Dyer, A. L.; Reynolds, J. R., Broadly absorbing black to transmissive switching electrochromic polymers. *Advanced Materials* **2010**, 22 (44), 4949-4953.

- [119] Jensen, J.; Dyer, A. L.; Shen, D. E.; Krebs, F. C.; Reynolds, J. R., Direct photopatterning of electrochromic polymers. *Advanced Functional Materials* **2013**, *23* (30), 3728-3737.
- [120] Yu, J.; Abley, M.; Yang, C.; Holdcroft, S., Chemically amplified photolithography of a conjugated polymer. *Chem. Commun.* **1998**, (15), 1503-1504.
- [121] Yang, K.; He, T.; Chen, X.; Cheng, S. Z.; Zhu, Y., Patternable Conjugated Polymers with Latent Hydrogen-Bonding on the Main Chain. *Macromolecules* **2014**, *47* (24), 8479-8486.
- [122] Leasure, R. M.; Ou, W.; Moss, J. A.; Linton, R. W.; Meyer, T. J., Spatial electrochromism in metallopolymeric films of ruthenium polypyridyl complexes. *Chemistry of materials* **1996**, *8* (1), 264-273.
- [123] Leizerson, I.; Lipson, S.; Lyushnin, A., Finger instability in wetting-dewetting phenomena. *Langmuir* **2004**, *20* (2), 291-294.
- [124] King Jr, C. R.; Sekar, D.; Bakir, M. S.; Dang, B.; Pikarsky, J.; Meindl, J. D. In *3D stacking of chips with electrical and microfluidic I/O interconnects*, Electronic Components and Technology Conference, 2008. ECTC 2008. 58th, IEEE: 2008; pp 1-7.
- [125] Nomerotski, A.; Buytart, J.; Collins, P.; Dumps, R.; Greening, E.; John, M.; Mapelli, A.; Leflat, A.; Li, Y.; Romagnoli, G., Evaporative CO₂ cooling using microchannels etched in silicon for the future LHCb vertex detector. *Journal of Instrumentation* **2013**, *8* (04), P04004.
- [126] Whitesides, G. M., The origins and the future of microfluidics. *Nature* **2006**, *442* (7101), 368-373.
- [127] Losey, M. W.; Jackman, R. J.; Firebaugh, S. L.; Schmidt, M.; Jensen, K. F., Design and fabrication of microfluidic devices for multiphase mixing and reaction. *Microelectromechanical Systems, Journal of* **2002**, *11* (6), 709-717.

- [128] Ayazi, F.; Najafi, K., A HARPSS polysilicon vibrating ring gyroscope. *Microelectromechanical Systems, Journal of* **2001**, 10 (2), 169-179.
- [129] Ayazi, F.; Najafi, K., High aspect-ratio combined poly and single-crystal silicon (HARPSS) MEMS technology. *Microelectromechanical Systems, Journal of* **2000**, 9 (3), 288-294.
- [130] Solak, H. H.; David, C.; Gobrecht, J.; Golovkina, V.; Cerrina, F.; Kim, S.; Nealey, P., Sub-50 nm period patterns with EUV interference lithography. *Microelectronic Engineering* **2003**, 67, 56-62.
- [131] Marty, F.; Rousseau, L.; Saadany, B.; Mercier, B.; Français, O.; Mita, Y.; Bourouina, T., Advanced etching of silicon based on deep reactive ion etching for silicon high aspect ratio microstructures and three-dimensional micro-and nanostructures. *Microelectronics journal* **2005**, 36 (7), 673-677.
- [132] Parasuraman, J.; Summanwar, A.; Marty, F.; Basset, P.; Angelescu, D. E.; Bourouina, T., Deep reactive ion etching of sub-micrometer trenches with ultra high aspect ratio. *Microelectronic Engineering* **2014**, 113, 35-39.
- [133] Chou, S. Y.; Krauss, P. R.; Renstrom, P. J., 25-nanometer resolution. *Science* **272** **1996**, 85-87.
- [134] Palik, E.; Bermudez, V.; Glembocki, O., Ellipsometric Study of Orientation - Dependent Etching of Silicon in Aqueous KOH. *Journal of the Electrochemical Society* **1985**, 132 (4), 871-884.
- [135] Lehmann, V.; Föll, H., Formation mechanism and properties of electrochemically etched trenches in n - type Silicon. *Journal of the Electrochemical Society* **1990**, 137 (2), 653-659.
- [136] Huang, Z.; Geyer, N.; Werner, P.; De Boor, J.; Gösele, U., Metal - assisted chemical etching of silicon: a review. *Advanced materials* **2011**, 23 (2), 285-308.

- [137] Li, L.; Li, B.; Lin, Z.; Wong, C.-P. In A low-cost fabrication route for silicon microchannels and microgratings with flow-enabled polymer self-assembly patterning and wet etching, *Electronic Components and Technology Conference (ECTC), 2015 IEEE 65th, IEEE: 2015*; pp 2149-2154.
- [138] Yeom, J.; Wu, Y.; Selby, J. C.; Shannon, M. A., Maximum achievable aspect ratio in deep reactive ion etching of silicon due to aspect ratio dependent transport and the microloading effect. *Journal of Vacuum Science & Technology B* **2005**, 23 (6), 2319-2329.
- [139] Li, L.; Wong, C.-P. In High-speed wet etching of through silicon vias (TSVs) in micro-and nanoscale, *Electronic Components and Technology Conference (ECTC), 2014 IEEE 64th, IEEE: 2014*; pp 631-635.
- [140] Hildreth, O. J.; Brown, D.; Wong, C. P., 3D Out - of - Plane Rotational Etching with Pinned Catalysts in Metal - Assisted Chemical Etching of Silicon. *Advanced Functional Materials* **2011**, 21 (16), 3119-3128.
- [141] Liyi Li, B. L., Chuchu Zhang, Chia-Chi Tuan, Zhiqun Lin*, Ching-Ping Wong*, A Facile and Low-Cost Route to High-Aspect-Ratio Microstructures on Silicon via a Judicious Combination of Flow-Enabled Self-Assembly and Metal-assisted Chemical Etching. manuscript to be submitted.
- [142] Mikhael, B.; Elise, B.; Xavier, M.; Sebastian, S.; Johann, M.; Laetitia, P., New silicon architectures by gold-assisted chemical etching. *ACS applied materials & interfaces* **2011**, 3 (10), 3866-3873.